UNIVERSITY OF CALIFORNIA, SAN DIEGO

Quantitative Radiographic Measures Derived from Automatic Segmentation of Glioblastoma Medical Imaging Associate with Patient Survival and Tumor Genomics

A dissertation submitted in partial satisfaction of the requirements for the degree Doctor of Philosophy

in

Neurosciences

by

Tyler C. Steed

Committee in charge:

Professor Clark C. Chen, Chair
Professor James B. Brewer
Professor Bob S. Carter
Professor Anders M. Dale
Professor Scott R. Vandenberg

2015

The Dissertation of Tyler C. Steed is approved, and it is acceptable in quality and form for publication on microfilm and electronically:

Chair

University of California, San Diego

2015

TABLE OF CONTENTS

Signature Page iii

Table of Contents iv

List of Abbreviations vi

List of Figures vii

List of Tables ix

Acknowledgements vi

Vita xi

Abstract of the Dissertation xiii

1. Introduction 1
2. Iterative probabilistic voxel labeling (IPVL): automated segmentation for analysis of The Cancer Imaging Archive (TCIA) glioblastoma images 4
   2.1. Introduction 6
   2.2. Materials and Methods 9
      2.2.1. The Cancer Imaging Archive (TCIA) 9
      2.2.2. Preprocessing 12
      2.2.3. Preliminary segmentation 12
      2.2.4. K-Nearest neighbor (KNN) and Gaussian mixture model (GMM) classifiers 14
      2.2.5. Final segmentation 15
      2.2.6. Segmentation evaluation 16
      2.2.7. Minimum image requirement for adequate segmentation 17
   2.3. Results 18
      2.3.1. Overview of automated segmentation algorithm 18
      2.3.2. Manual segmentation comparison 20
      2.3.3. Minimal image requirement for adequate segmentation 25
   2.4. Discussion 28
   2.5. Conclusions 31
3. Differential localization of glioblastoma subtype implicates the sub-ventricular zone (SVZ) in glioblastoma pathogenesis 32
   3.1. Introduction 34
   3.2. Materials and Methods 36
      3.2.1. Data acquisition and Subtype Classification 36
      3.2.2. Image Preprocessing and Registration 36
      3.2.3. Tumor Segmentation and Probability Maps 37
      3.2.4. Subventricular Zone Distance 39

3.2.5. ssGSEA and Statistical Analyses 39
3.3. Results 40
3.3.1. Glioblastoma Density Map 40
3.3.2. Glioblastoma Subtype Specific Density Maps 43
3.3.3. The SVZ Distance 46
3.3.4. SVZ Distance and Glioblastoma Biology 48
3.3. Discussion 50
3.4. Conclusions 52
4. Quantification of lateral ventricular displacement magnitude in glioblastoma imaging from the TCIA is associated with patient survival 53
4.1. Introduction 55
4.2. Materials and Methods 57
4.2.1. Data acquisition and Imaging 57
4.2.2. Image Preprocessing and Registration 57
4.2.3. Tumor Segmentation and Probability Maps 58
4.2.4. Subventricular Zone Distance 58
4.2.5. Lateral Ventricular Displacement 58
4.3. Results 61
4.3.1. LVd shifts occur in a majority of glioblastoma tumor patients 61
4.3.2. The variance of LVd is not solely explained by tumor volume 65
4.3.3. Glioblastoma patients with higher LVd demonstrate poorer survival 67
4.3.4. Differential expression analysis identifies that biosynthetic pathways, and genes tied to oxidative phosphorylation are upregulated, while neural differentiation factors are downregulated in tumors with high LVd. 70
4.4. Discussion 72
5. Conclusions and Future Studies 77

References 79

LIST OF ABBREVIATIONS

BV	blood vessel
CEV	contrast-enhancing volume
CoM	center of mass
DICE	Dice similarity coefficient
FHV	FLAIR hyperintensity volume
FLAIR	fluid level attenuated inversion recovery
GBM	glioblastoma multiforme
G-CIMP	CpG Island methylator phenotype
GMM	Gaussian mixture modeling
IPVL	Iterative Probabilistic Voxel Labeling
KNN	k-nearest neighbor
mSigDB	Molecular Signatures Database
T1wCE	T1-weighted image with contrast
LvD	lateral ventricular displacement
REMBRANDT	Repository for Molecular Brain Neoplasia Data
SVZ	subventricular zone
SVZd	subventricular zone distance
TCGA	The Cancer Genome Atlas
TCIA	The Cancer Imaging Archive

LIST OF FIGURES

Figure 2.1 19
Work flow for Iterative Probabilistic Voxel Labeling (IPVL). (A) Downloaded TCIA images were preprocessed. (B) Preliminary segmentation was performed to generate conservative yet highly specific preliminary volumes. (C) In the classification step, these volumes were used to train the GMM and KNN probabilistic classifiers. The…

Figure 2.2 23
IPVL segments volumes that are highly analogous to operator-defined volumes. Results from 4 subjects representing the highest and lowest Dice similarity coefficient (DICE) scores for CEV and FHV segmentations are shown. (A) The highest DICE (top) and lowest DICE (bottom) examples of IPVL-segmented CEVs relative to…

Figure 2.3 24
Quantitative comparison between IPVL-defined volumes and operator-derived volumes compared with interoperator comparisons. (A and B) DICE comparisons for 2 sets of IPVL-defined and operator-defined CEVs are shown. DICE scores were calculated comparing CEVs generated by IPVL, operator 1, and operator 2. (C…

Figure 2.4 27
Effects of removing image sequences on IPVL segmentation. (A) Select image sequences (such as T1WI) were removed before IPVL CEV segmentations for each subject. The image sequences that were available during IPVL segmentation are indicated by a plus sign. DICE scores were calculated for the resultant CEVs…

Figure 3.1 38
Workflow for generation of total CE and centroid density maps. Preprocessed images (A) were registered to the Montreal Neurological Institute (MNI) template and segmented according to the IPVL pipeline (B). CE volumes were filled (C) and centroid of each were calculated (D). Filled CE volumes from each subject were…

Figure 3.2 42
Radiographic glioblastoma density map. Total CE probability map revealed that glioblastoma, as a whole, exhibit a strong predilection occurrence in proximity to the SVZ. Red indicates the highest frequency of overlap and light-blue indicating the lowest frequency of overlap.

Figure 3.3 45
Glioblastoma subtype density maps. Subtype-specific density maps were generated using total CE volume. Red indicates the highest frequency of overlap and light-blue indicating the lowest frequency of overlap.

Figure 3.4 45
Regions of statistically significant subtype localization. Axial (first row) and sagittal (second row) of statistically significant clusters ($p < 0.05$) by subtype. Statistical comparisons were carried out using voxel-wise Fisher's exact tests.

Figure 3.5 47
Association of SVZ distance with overall survival and CD133 gene expression. (A) Graphical illustration of the SVZ distance measurement. SVZ distance is color coded so that blue indicates shorter SVZ distances while red indicates high SVZ distances. (B) Kaplan Meier Survival curve demonstrating association of lower SVZ distance… subtypes.

Figure 4.1 60
Illustrative flow of Lateral Ventricular displacement (LVd) calculation. Top: Images are automatically segmented into the constituent tissue compartments to extract the CSF volume in patients with tumor. Bottom: The same segmentation is performed on the MNI template to derive a theoretical "normal" CSF volume. The…

Figure 4.2 63
Patients with similar tumor volumes can have differing levels of LVd. Examples from a MNI axial slice z=87 representing the range of CSF displacement magnitudes from the TCGA cohort. Red indicates the borders of the T1wCE CSF lateral ventricular segmentation, while yellow indicates the segmentation of the MNI lateral ventricles…

Figure 4.3 64
LVds occur in a majority of glioblastoma tumor patients. Right: Boxplot illustrating the difference in mean and variance of LVd in both normal and tumor cohorts. glioblastoma tumors showed a significantly higher mean LVd. ** $p < .0001$. Left: Histogram demonstrating the distribution of LVd magnitude in a normal cohort…

Figure 4.4 66
Subjects with similar tumor volumes can have differing levels of LVd. Examples a MNI axial slice z87 representing the range of CSF displacement magnitudes from the TCGA cohort. Red indicates the borders of the T1wCE CSF lateral ventricular segmentation, while yellow indicates the segmentation of the MNI lateral ventricles…

Figure 4.5 68
Increased LVd is a strongly associated with poorer patient survival and increased SVZ distance is a strongly associated with longer patient survival. Left: Kaplan-Meier survival curve derived from a median cutoff of LVd distribution in the TCGA cohort. Higher levels of LVd are associated with decreased survival (p=0.02 log rank, n=...

Figure 4.6 71
Differential expression analysis reveals genes associated with LVd: Volcano plot illustrating the genes upregulated in high LVd (at right in red), and genes downregulated in high LVd (at left in green). Log 2 of fold change is denoted on the x- axis.

LIST OF TABLES

Table 2.1..... 10
Site, scanner, and image information for the TCIA subjects analyzed in the initial cohort.

Table 2.2..... 11
Site, scanner, and image information for the TCIA subjects analyzed in the validation cohort.

Table 3.1..... 41
Summary of demographic data, clinical outcome, and radiographic CE volume.

Table 4.1..... 69
Cox Regression analysis with LVd, SVZd, and age

ACKNOWLEDGEMENTS

When I began my rotation in Clark Chen's lab at Moores Cancer Center, I didn't know that was where I would ultimately pursue my PhD. As the only graduate student in the lab, I was impressed with the high-quality young postdocs and an enthusiastic, driven PI whose passion for science was clearly evident. Their passion and dedication quickly began to inspire my work in a field I had yet to explore and made my decision to stay an easy one. I would like to thank the postdocs who have mentored my work and developed my understanding of molecular biology, writing, and scientific thinking. I could not have been successful in my studies if not for the efforts and patience of my colleagues and dear friends, Valya Ramakrishnan, Jie Li, Johnny Akers, and Ying Shen. Their intelligence, kindness, and passion for quality work will undoubtedly lead each of them to their future academic goals.

I would like to thank Dr. Chen for his gracious invitation for me to join his lab, and for his refusal to accept anything but my best efforts. Within a year of joining the lab when I decided to embark on a project outside of our main focus, he willingly supported me to pursue my own project direction by allowing me to work on a thesis investigating the neuroimaging correlates of glioblastoma. His willingness to explore new angles and take risks, his refusal to accept anything short of maximal effort, and his dedication to his lab, students, patients, and family are all truly admirable qualities that I will strive to emulate in my future career.

During my time in the lab, I was blessed to have wonderful dedicated students that Dr. Chen encouraged me to mentor. These students, each immensely gifted in their own right, have helped me to grow as a mentor and have taught me so much more than I can hope to have taught them. Therefore, I would like to thank Jeff Treiber, Zack Taich, and Kunal Patel for their tireless efforts, intellectual contributions, and most of all, their friendship.

I would also like to acknowledge and thank each of the members of my thesis committee, which includes Scott Vandenberg, Jim Brewer, Bob Carter, and Anders Dale. Each of these members have generously contributed their time, resources, and efforts to ensure my great doctoral training and mentoring. Their germane and astute scientific assessments in addition to wise career advice have been instrumental to my development.

I would like to thank Anders Dale and the Multi Modal Imaging Laboratory for the gracious hospitality they showed by providing a workstation and the support necessary to perform the neuroimaging studies which comprise the backbone of my thesis.

I am truly fortunate to be a member of the UC San Diego Medical Scientist Training Program, and would therefore like to thank the MSTP director Paul Insel and the program's stalwart Program Manager Mary Alice Kiisel. Their direction and encouragement along with the camaraderie of my classmates in the program were essential to completing my PhD, and I pray will continue to aid me as I return to the final years of my medical education. I would also like to thank Kent Lam, an MSTP friend and colleague, who worked

alongside our lab at Moores Cancer Center. He was a constant source of advice, encouragement, and material, who even helped provide his thesis dissertation as a template.

I extend my thanks to the excellent coordinators of the Neurosciences Graduate Program, including Erin Gilbert and Linh Vandermar, who were always available for questions and were attentive to student needs and concerns.

I am blessed to have a loving and compassionate family. My lifelong friends Taylor Geron and David Carlon, have been constant sources of motivation and support. My loving brother, Camden, always finds a way to uplift my spirits and is generous with his time when any help is needed. His company is a constant source of renewal each time I spend time with him.

I would like to thank my inspiring mom, Shay Steed, an exceptional high school social studies teacher. Her toughness, perseverance, and patience while raising two boys never detracted from her infectious charity and compassion. I learned my desire for service from her, and her sense of compassion is something I try to bring to every patient I encounter. I thank her for all the sacrifices she made to allow me to pursue my goals and dreams. Because of her efforts, I am a proud alumnus of UC Berkeley, an inspired teacher, and a caring husband. Her support throughout my academic pursuits has been essential, and I aspire to be as loving and supportive a parent as the example she has set.

Finally, I would like to acknowledge the ineffable contributions of my dear wife and best friend, Danielle. Without her constant support and her efforts, I could not dream of making it to where I find myself today. Despite her own challenges with graduate training, she generously offers her help without hesitation, serving as my editor-in-chief, scientific consultant, and source of confidence. With her support, I know that, whatever challenges lie ahead, I possess the will and means to take them head on.

Chapter 2, in its entirety, was accepted to the American Journal of Neuroradiology for publication. Tyler C. Steed, Jeffrey M. Treiber, Kunal S. Patel, Zach Taich, Nate S. White, Michelle L. Treiber, Nikdokht Farid, Bob S. Carter, Anders M. Dale, and Clark C. Chen. “Iterative probabilistic voxel labeling (IPVL): automated segmentation for analysis of The Cancer Imaging Archive (TCIA) glioblastoma images.” The dissertation/thesis author was the primary investigator and author of this paper.

Chapter 3, in part, is currently in preparation for submission for publication of the material. Tyler C. Steed, Jeffrey M. Treiber, Kunal S. Patel, Bob S. Carter, Anders M. Dale, and Clark C. Chen. Tentatively entitled “Differential localization of glioblastoma subtype implicates the sub-ventricular zone (SVZ) in glioblastoma pathogenesis.” The dissertation/thesis author was the primary investigator and author of this material.

Chapter 4, in part, is now in preparation for submission for publication of the material. Tyler C. Steed, Jeffrey M. Treiber, Kunal Patel, Bob S. Carter, Anders M. Dale, and Clark C. Chen (2014). Tentatively entitled “Quantification

of lateral ventricle displacement magnitude in glioblastoma imaging associates with decreased patient survival. The dissertation/thesis author was the primary investigator and author of this material.

VITA

2009 Bachelor of Arts in Molecular and Cell Biology, University of California, Berkeley

2015 Doctor of Philosophy, University of California, San Diego

2017 (Expected) Medical Doctor, University of California, San Diego

PUBLICATIONS

1. **Steed, T. C.**, J. M. Treiber, K. S. Patel, B. S. Carter, A. M. Dale, and C. C. Chen (2015). "Quantification of lateral ventricle displacement magnitude in glioblastoma imaging associates with decreased patient survival." In preparation.

2. **Steed, T. C.**, J. M. Treiber, K. S. Patel, B. S. Carter, A. M. Dale, and C. C. Chen (2015). "Quantification of glioblastoma spatial localization reveals associations with molecular subtypes and implicates the subventricular zone in tumor pathogenesis." In preparation.

3. Rodriguez, R. A., D. B. Steed, Y. Kawamata, S. Su, P. A. Smith, **T. C. Steed**, F. E. Romesberg, and P. S. Baran (2014). Axinellamines as broad spectrum antibacterial agents: scalable synthesis and biology." *J Am Chem Soc* 136 (43):15403–15413

4. Treiber, J. M., N. White, **T.C. Steed**, H. Bartsch, B. S. Carter, A. M. Dale, and C. C. Chen (2014). "Characterization and correction of geometric distortions in diffusion weighted imaging (DWI): A study of 756 neurosurgical images." In submission, *Neurosurgery*.

5. **Steed, T. C.**, J. M. Treiber, K. S. Patel, Z. Taich, N. S. White, M.L. Treiber, N. Farid, B. S. Carter, A. M. Dale, and C. C. Chen (2014). Iterative probabilistic voxel labeling (IPVL): automated segmentation for analysis of The Cancer Imaging Archive (TCIA) glioblastoma images." *Am J Neuroradiol*. 10.3174/ajnr.A4171.

6. Shen, Y., M. Nitta, J. Li, D. Futalan, **T. Steed**, Z. Taich, J. M. Treiber, D. Stevens, J. Wakosky, H.-Z. Chen, B. S. Carter, F. Esashi, J. N. Sarkaria, F. B. Furnari, W. K. Cavenee, A. Desai, and C. C. Chen (2014). "Bypassing resistance to EGFR inhibitors by synthetic lethality in glioblastoma." In submission.

7. Kushwaha, D., V. Ramakrishnan, K. Ng, **T. Steed**, T. Nguyen, D. Futalan, J. C. Akers, J. Sarkaria, T. Jiang, D. Chowdhury, B. S. Carter and C. C. Chen (2014). "A genome-wide miRNA screen revealed miR-603 as a MGMT-regulating miRNA in glioblastomas." *Oncotarget* 5(12): 4026-4039.

8. Li, J., S. Zhu, D. Kozono, K. Ng, D. Futalan, Y. Shen, J. C. Akers, **T. Steed**, D. Kushwaha, M. Schlabach, B. S. Carter, C. H. Kwon, F. Furnari, W. Cavenee, S. Elledge and C. C. Chen (2014). "Genome-wide shRNA screen revealed integrated mitogenic signaling between dopamine receptor D2 (DRD2) and epidermal growth factor receptor (EGFR) in glioblastoma." *Oncotarget* 5(4): 882-893.

9. Nizar, K., H. Uhlirova, P. Tian, P. A. Saisan, Q. Cheng, L. Reznichenko, K. L. Weldy, **T. C. Steed**, V. B. Sridhar, C. L. MacDonald, J. Cui, S. L. Gratiy, S. Sakadzic, D. A. Boas, T. I. Beka, G. T. Einevoll, J. Chen, E. Masliah, A. M. Dale, G. A. Silva and A. Devor (2013). "In vivo stimulus-induced vasodilation occurs without IP3 receptor activation and may precede astrocytic calcium increase." *J Neurosci* 33(19): 8411-8422.

10. Furst, A. J., G. D. Rabinovici, A. H. Rostomian, **T. Steed**, A. Alkalay, C. Racine, B. L. Miller, W. J. Jagust (2010). “Cognition, glucose metabolism and amyloid burden in Alzheimer's disease.” *Neurobiol Aging* 33(2):215-25.

FIELDS OF STUDY

Major Field: Neurosurgery (Neuro-Oncology)

ABSTRACT OF THE DISSERTATION

Radio-Genomics of Glioblastoma

by

Tyler C. Steed

Doctor of Philosophy in Neurosciences

University of California, San Diego, 2015

Professor Clark C. Chen, Chair

Glioblastoma, the most common and deadly form of primary brain cancer, is characterized by rapid progression, heterogeneity, and defiance of therapy. The relentless nature of glioblastoma emphasizes the urgency of identifying improved methods to hasten the development of tailored treatments for patients afflicted by this malignancy. Genetic profiling of clinical glioblastoma specimens has revealed that glioblastoma, like other cancers, is composed of many different subtypes that may possess unique sensitivities to therapeutics. To improve the clinical outcome of glioblastoma patients,

technologies must be developed to better define and discriminate the subtypes of glioblastomas in an affordable, accurate, and noninvasive manner.

The heterogeneity of glioblastoma's genomic and molecular alterations mirror the diversity of its appearance in medical imaging. The emerging field of radiogenomics integrates methods common to neuroimaging, bioinformatics, and molecular biology to identify the radiographic correlates of tumor cellular and molecular processes. Application of radiogenomics to the study of glioblastoma may facilitate its understanding, especially when considering that magnetic resonance (MR) imaging is required for the modern clinical management of this disease. Unfortunately, radiogenomic progress demands accurate and high-throughput methods to reliably segment features from vast and varied imaging archives, and the careful design of metrics which capture biological phenotypes.

In this context, we developed a robust algorithm for tumor segmentation and radiophenotype parameterization termed Iterative Probabilitic Voxel Labeling (IPVL). Application of IPVL to glioblastoma tumor images from The Cancer Imaging Archive (TCIA) with associated genomic profiling available via The Cancer Genome Atlas (TCGA) led to the topographic mapping of glioblastoma spatial distributions by molecular subtype, and the discovery of two survival-associated radiographic parameters. These parameters, tumor subventricular distance (SVZd), and lateral ventricle displacement (LVd), correlate with defined physiologic mechanisms, and associated genomic profiles. Together, these results provide

proof of principle that quantitative radiographic assessment of glioblastoma is a viable and effective strategy capable of augmenting the power of molecular and genomic research. With further study in the clinical setting, application of these methodologies and novel imaging parameters could impact prognostic evaluation, identify tumor therapeutic subgroups, and hopefully improve the lives of patients.

1. Introduction

Glioblastoma multiforme (GBM), the most common and most lethal form of primary brain tumor exhibits remarkable heterogeneity and resistance to therapy [1]. Despite aggressive treatment which includes surgical resection, radiation therapy, and chemotherapy, the median survival of patients afflicted with this condition remains 12-15 months [2], largely a result of tumor, histological, and genomic heterogeneity [3]. This heterogeneity persists from its appearance on imaging down to the molecular alterations present in each constituent cell, presenting significant obstacles to those who hope to understand the mechanisms governing its pathophysiology. In an effort to better understand the variability of glioblastoma, TCGA, a worldwide consortium of cancer researchers and clinicians selected glioblastoma to be the first target for their interdisciplinary approach [4]. To date, the TCGA has collected over 500 clinical tumor specimens, while consolidating genomic profiling, clinical information, neuroimaging, and histopathology into publicly available databases. This work has led to the discovery of at least five distinct subtypes of glioblastoma characterized by genomic expression and epigenetic changes. These subtypes include the proneural, neural, classical, mesenchymal, and the glioma-methylation CpG island profile phenotype (G-CIMP), which is associated with improved patient survival [5]

The modern clinical management of glioblastoma requires magnetic resonance imaging (MRI), which is used to diagnose glioblastoma, monitor

therapeutic response, and aid in surgical resection. This abundance of MR imaging presents a potential wealth of data which may be harnessed to better characterize and understand the landscape of glioblastoma variation. Over the last decade, the rise of genomic profiling, the increase in digital imaging availability, and the exponential growth of computing power and data storage has fostered the maturation of radiogenomics [3], a field which aims to characterize the relationships between radiographic imaging and genomic alterations.

Significant obstacles have impeded the study of tumor neuroimaging archives. The radical distortions that tumors cause in patients' brains also wreak havoc on the majority of tools designed for neuroimaging analysis and processing of normal brains. Additionally, as a result of many different hospitals contributing to the TCIA and a more general lack of standardized imaging methodologies, the TCIA is a widely varied imaging cohort requiring careful handling to perform robust imaging analysis.

The parameterization of glioblastoma MRI may offer a glimpse into the pathophysiology of a tumor and its progression, and help guide clinical decision making as we proceed toward more individualized approaches. In order to address the challenges and discover the genomic correlates of radiographic features in glioblastomas, new tools for both the segmentation and evaluation of brain tumor associated volumes were designed and are subsequently outlined here. The automatic preprocessing and segmentation method Iterative Probabilistic Voxel Labeling (IPVL) is a reliable and robust

tool for segmentation of glioblastoma associated volumes. Furthermore, this thesis will demonstrate that application of IPVL facilitated the study of the spatial distribution of glioblastomas by molecular subtype, and helped discover two novel survival-associated radiographic parameters: tumor subventricular distance and lateral ventricle displacement.

2. Iterative probabilistic voxel labeling (IPVL): automated segmentation for analysis of The Cancer Imaging Archive (TCIA) glioblastoma images

BACKGROUND AND PURPOSE: Robust, automated segmentation algorithms are required for quantitative analysis of large imaging datasets. We developed an automated method that identifies and labels brain tumor–associated pathology by using an iterative probabilistic voxel labeling using k-nearest neighbor and Gaussian mixture model classification. Our purpose was to develop a segmentation method which could be applied to a variety of imaging from The Cancer Imaging Archive.

MATERIALS AND METHODS: Images from 2 sets of 15 randomly selected subjects with glioblastoma from The Cancer Imaging Archive were processed by using the automated algorithm. The algorithm-defined tumor volumes were compared with those segmented by trained operators by using the Dice similarity coefficient.

RESULTS: Compared with operator volumes, algorithm-generated segmentations yielded mean Dice similarities of 0.92 ± 0.03 for contrast-enhancing volumes and 0.84 ± 0.09 for FLAIR hyperintensity volumes. These values compared favorably with the means of Dice similarity coefficients

between the operator-defined segmentations: 0.92 ± 0.03 for contrast-enhancing volumes and 0.92 ± 0.05 for FLAIR hyperintensity volumes. Robust segmentations can be achieved when only postcontrast T1WI and FLAIR images are available.

CONCLUSIONS: Iterative probabilistic voxel labeling defined tumor volumes that were highly consistent with operator-defined volumes. Application of this algorithm could facilitate quantitative assessment of neuroimaging from patients with glioblastoma for both research and clinical indications.

2.1. Introduction

Glioblastoma is the most common primary brain tumor and remains one of the deadliest human cancers [6]. During the past 50 years, improvement with regard to patient outcomes has been marginal [7]. A major barrier in therapeutic development is attributable to the misconception that glioblastoma constitutes a single disease. Molecular profiling has revealed that glioblastoma comprises multiple subtypes characterized by distinct molecular pathways [8]. To improve the clinical outcome of patients with glioblastoma, technologies must be developed to distinguish these subtypes.

There are compelling reasons that MR imaging may serve as a tool for dissecting the variability of glioblastoma. First, radiographic data are available for every patient because the clinical management of glioblastoma tumors is largely driven by the interpretation of MR images. Second, available data suggest that the radiographic appearance of glioblastoma is related to its physiologic state [9, 10] To better define this relationship, imaging archives with corresponding genomic profiling, such as The Cancer Imaging Archive (TCIA), have been launched (http://cancerimagingarchive.net/).

Much of the early work correlating MR imaging appearances of glioblastoma tumors with genomic profiling was performed by using manually delineated tumor volumes or qualitative assessments provided by trained clinicians [9, 10]. These approaches are limited by the inherent variability of subjective interpretation, and significant interrater discrepancies have been

reported [11, 12]. Additionally, manual segmentation is time-consuming for large datasets. This limitation is particularly apparent when multiple radiographic features require segmentation. To address these deficiencies, effort has been devoted to developing automated algorithms for segmenting tumor volumes [13-17]. These algorithms include clustering [18, 19], discriminative strategies [20], and generative approaches [16, 21, 22]. The success of these methods has been limited by widely differing MR imaging protocols for image acquisition and quality [23] and the significant overlap between the radiographic appearance of glioblastoma tumors and normal cerebrum on MR imaging. Although many of these methods can generate high-quality volumes from a training set, segmentation algorithms may fail when applied to images acquired by using different protocols.

We hypothesized that a probabilistic approach by using subject specific classifiers would reliably discriminate glioblastoma from the surrounding cerebrum. In this algorithm, termed iterative probabilistic voxel labeling (IPVL), sparse, high-specificity, preliminary volumes were created for each subject by using a combination of region growing and K-means-based tissue segmentation. Sampling of these preliminary volumes trained k-nearest neighbor (KNN) and Gaussian mixture model (GMM) classifiers by using voxel intensity and spatial coordinates. Voxel labels are assigned probabilistically by iteratively trained classifiers. Finally, each voxel is labeled as contrast enhancing tumor volume (CEV), FLAIR hyperintensity volume (FHV), gray matter, white matter, CSF, and blood vessel (BV). Most important, our

algorithm reliably segments images from the TCIA that were acquired by a variety of scanners and protocols.

2.2. Materials and Methods

2.2.1. The Cancer Imaging Archive (TCIA)

MR images of glioblastoma tumors from The Cancer Imaging Archive were downloaded in June 2013. We identified subjects who underwent MR imaging before surgery and had a full complement of imaging, including the following: T1-weighted imaging, T1-weighted imaging with contrast enhancement (T1wCE), T2-weighted imaging, and FLAIR. Subjects were excluded when images contained a prohibitive amount of motion or distortion artifacts. Our algorithm was developed in a "pilot" set of 10 subjects from the TCIA. The algorithm was tested in 2 sets of 15 subjects selected from the TCIA that were not used during development. TCIA MR images were acquired from a number of institutions whose scanners differed by manufacturer and model and whose images varied by sequence, quality, and spatial resolution (**Tables 2.1 and 2.2**).

Table 2.1. Site, scanner, and image information for the TCIA subjects analyzed in the initial cohort.

				T1wCE		FLAIR	
Subject	Site	Scanner	Year	Resolution (mm^2)	Section Thickness (mm)	Resolution (mm^2)	Section Thickness (mm)
TCGA-02–0033	MD Anderson Cancer Center	Genesis Signa 1.5T[a]	1997	0.78 × 0.78	6.5	0.78 × 0.78	6.5
TCGA-02–0048	MD Anderson Cancer Center	Genesis Signa 1.5T	1999	0.98 × 0.98	1.5	0.78 × 0.78	6.5
TCGA-02–0064	MD Anderson Cancer Center	Signa Excite 3T[a]	1999	0.47 × 0.47	6.5	0.94 × 0.94	2
TCGA-02–0068	MD Anderson Cancer Center	Signa Excite 1.5T	2000	0.86 × 0.86	6.5	0.86 × 0.86	6.5
TCGA-02–0075	MD Anderson Cancer Center	Signa Excite 3T	1999	0.86 × 0.86	1.5	0.86 × 0.86	6.5
TCGA-06–0137	Henry Ford Hospital	NA	2001	0.94 × 0.94	3	0.94 × 0.94	3
TCGA-06–0139	Henry Ford Hospital	NA	2004	0.47 × 0.47	2.5	0.47 × 0.47	2.5
TCGA-06–0143	Henry Ford Hospital	NA	2005	0.47 × 0.47	3	0.47 × 0.47	2.5
TCGA-06–0154	Henry Ford Hospital	NA	1996	0.94 × 0.94	3	0.94 × 0.94	3
TCGA-06–0164	Henry Ford Hospital	NA	1999	0.94 × 0.94	3	0.94 × 0.94	3
TCGA-08–0358	UCSF Med. Ctr.	Genesis Signa 1.5T	2002	1.02 × 1.02	1.5	0.86 × 5	0.86
TCGA-14–1794	Emory Univ.	Intera 1.5T[b]	1998	0.45 × 0.45	6	0.45 × 0.45	6
TCGA-15–2714	Mayo Clinic	Signa Excite 1.5T	1996	0.86 × 0.86	4	0.86 × 0.86	4
TCGA-76–5384	Thomas Jefferson Univ.	Magnetom Vision 1.5T[c]	2000	0.86 × 0.86	7.5	0.86 × 0.86	7.5
TCGA-76–6190	Thomas Jefferson Univ.	Magnetom Vision 1.5T	1998	0.47 × 0.47	1.5	0.86 × 0.86	7.5

Note:—UCSF Med. Ctr. indicates University of California, San Francisco Medical Center; Univ., University; NA, not applicable.

[a] GE Healthcare, Milwaukee, Wisconsin.

[b] Philips Healthcare, Best, the Netherlands.

[c] Siemens, Erlangen, Germany.

Table 2.2. Site, scanner, and image information for the TCIA subjects analyzed in the validation cohort.

				T1wCE		FLAIR	
Subject	Site	Scanner	Year	Resolution (mm^2)	Section Thickness (mm)	Resolution (mm^2)	Section Thickness (mm)
HF1058	Henry Ford Hospital (REM)	NA	1992	0.94 × 0.94	3.0	0.78 × 0.78	3.0
HF1139	Henry Ford Hospital (REM)	NA	1993	0.94 × 0.94	3.0	0.94 × 0.94	3.0
TCGA-06–0166	Henry Ford Hospital	Genesis Signa 1.5T	2004	0.94 × 0.94	3.0	0.94 × 0.94	3.0
TCGA-06–0187	Henry Ford Hospital	NA	2004	0.94 × 0.94	2.5	0.94 × 0.94	2.5
TCGA-06–0190	Henry Ford Hospital	NA	2004	0.94 × 0.94	2.5	0.94 × 0.94	2.5
TCGA-06–0646	Henry Ford Hospital	NA	2005	0.47 × 0.47	2.5	0.47 × 0.47	2.5
TCGA-06–5413	Henry Ford Hospital	NA	2008	0.47 × 0.47	2.5	0.47 × 0.47	2.5
TCGA-19–2631	Case Western	Avanto 1.5T[a]	2003	1.00 × 1.00	1.0	0.90 × 0.90	5.5
TCGA-76–5385	Thomas Jefferson Univ.	Magnetom Vision 1.5T	2000	0.51 × 0.51	1.5	0.86 × 0.86	7.5
TCGA-76–5386	Thomas Jefferson Univ.	Achieva 1.5T[b]	2000	0.86 × 0.86	7.0	0.86 × 0.86	6.0
TCGA-76–5387	Thomas Jefferson Univ.	Achieva 3T	2001	0.45 × 0.45	5.0	0.69 × 0.69	6.0
TCGA-76–6192	Thomas Jefferson Univ.	Magnetom Vision 1.5T	2001	0.50 × 0.50	1.5	0.86 × 0.86	7.5
TCGA-76–6280	Thomas Jefferson Univ.	Achieva 1.5T	1998	0.94 × 0.94	1.5	0.86 × 0.86	6.0
TCGA-76–6288	Thomas Jefferson Univ.	Achieva 3T	2001	0.75 × 0.75	1.0	0.67 × 0.67	1.0
TCGA-76–6663	Thomas Jefferson Univ.	Achieva 3T	2001	0.75 × 0.75	1.0	0.69 × 0.69	6.0

Note:—HF indicates Henry Ford Hospital patients within the Repository for Molecular Brain Neoplasia Data (REMBRANDT) https://caintegrator.nci.nih.gov/rembrandt/; REM, REMBRANDT cohort subject; NA, not applicable.

[a] Siemens, Erlangen, Germany.

[b] Philips Healthcare, Best, the Netherlands.

2.2.2. Preprocessing

Images were preprocessed by using a combination of in-house and external software including the FMRIB Software Library [24, 25] (FSL, Version 5.0; http://fsl.fmrib.ox.ac.uk/fsl). Image distortions caused by gradient nonlinearity warping were corrected by using previous methods [26-28], followed by bias-field correction by using the FMRIB Automated Segmentation Tool (FAST) [29], and were registered to the Montreal Neurological Institute-152 nonlinear sixth-generation standard brain image [30]. Affine registration was performed by using the FMRIB Linear Image Registration Tool (FLIRT) [31, 32]. To ensure removal of nonbrain tissues (eg, skull, optic nerve, and carotid arteries), we created a stringent brain mask from the T1WI by using a modified combination of the FSL Brain Extraction Tool [29] and the Robust Brain Extraction tool (https://www.nitrc.org/projects/robex) [33]. Briefly, this method automatically compared the resultant brain with the volume derived from applying the Montreal Neurological Institute brain mask. Overestimation of >10% would adjust the fractional intensity, resulting in more restrictive brain outlines.

2.2.3. Preliminary segmentation

It was crucial to generate highly specific volumes that accurately represented the range of intensity and spatial distribution for each tissue label to appropriately train our segmentation algorithm to recognize each subject's features. After skull stripping, initial tissue segmentation into preliminary WM,

GM, CSF, and CEVs was performed for the available T1WI sequences by using FAST [29]. The FAST-derived initial CEV consisted of both tumor-associated CEV and BV volumes. The preliminary BV volume was distinguished from the FAST-derived CEV by performing 2 morphology-based manipulations. First, CEV objects located near the cortical surface were selectively removed by using a uniform spheric 3-mm erosion of the brain mask applied to the FAST-derived CEVs. Large vessels, such as the dural veins and carotid arteries, were removed by this operation due to their proximity to the brain surface. Second, a modified region growing algorithm was used to identify vessels that were continuous with the venous sinuses. Region-growing was seeded in the region of the torcula (confluence of the sinuses), which was identified on the template image, to which all images were registered. Voxels identified as vessels by the combination of these methods were labeled as preliminary BV volume, while the remaining CEV was assigned to preliminary tumor-associated CEV.

The FHV preliminary volume was created by first determining and applying an automatic threshold for the FLAIR image by using the Otsu method [34] FLAIR hyperintense regions on MR imaging may be tumor-associated or non-tumor-associated (eg, periventricular or pericortical). The non-tumor-associated hyperintense elements were excluded by using a spheric 3-mm erosion performed on the brain mask, while spheric 3-mm dilation was performed on the CSF volume. Together, these operations removed pericortical hyperintensities and the periventricular hyperintensities

from the remainder of the preliminary FHVs.

Approximately 25% of voxels were labeled at this time.The voxels labeled were randomly sampled from regions that had the highest specificity to a particular volume of interest. For contrast enhancement, these included regions of contrast enhancement not continuous with the sagittal and transverse sinus. For FLAIR hyperintensity, these included regions above an intensity threshold >1.5 SDs above the mean intensity of the FLAIR image. The voxels assigned to each preliminary tissue label were used as the basis for training probabilistic classifiers (KNN and GMM). Voxels that were not classified into these categories during preliminary volume segmentation remained unassigned to avoid adding noise to the classifiers.

2.2.4. K-Nearest neighbor (KNN) and Gaussian mixture model (GMM) classifiers

The classifiers used to assign voxel membership were KNN and GMM. The KNN algorithm is a nonparametric method that assigns membership of a single datum on the basis of a number of neighboring training examples [35, 36]. GMM allows statistical clustering of data into a predefined number of Gaussian distributions, which, in this case, represent distinct imaging features. Use of these 2 probabilistic classifiers was complementary.

To expedite processing and improve accuracy, we used a weighted random sampling of the preliminary volume voxels to train both KNN and GMM classifiers. The weights for sampling reflected the relative distribution of

voxels assigned to tissue labels from preliminary segmentation. Weighting was performed to avoid biasing the classifiers toward any particular tissue label caused by overrepresentation attributed to sampling error. Training was performed on a subject-by-subject basis, meaning that each patient was segmented according to his or her own subject specific classifier by using both intensity and spatial data from each voxel to define labels. After training, all voxels, including those that were unassigned during preliminary volume creation, were classified independently by both KNN and GMM probabilistically to the 6 tissue labels: CEV, FHV, CSF, GM, WM, and BV. The probability of membership for each voxel was determined by a distance metric from classifier training. For each voxel, the greatest tissue label probability determined voxel labeling. Classifier consensus was resampled and used to re-train another iteration of KNN classification at a higher voxel sampling rate. This step had the benefit of reducing noise introduced during the creation of preliminary volumes, improving both the smoothness of the final volumes and the accuracy of the tissue labels.

2.2.5. Final segmentation

Voxel label probabilities from all classifiers were summed, including the iterative KNN classification, for each tissue label, and a final segmentation volume was created by assigning voxels according to the highest probability membership to each tissue label. At this time, all voxels were probabilistically assigned. A voxel continuity filter was applied that removed discontinuous

clusters of limited connectivity (fewer than 150 contiguous voxels). To address voxels that had equal probabilities of belonging to ≥2 tissue labels, we set priority in the following manner from greatest to least: CEV > FHV > BV to ensure that individual voxel tissue labels were mutually exclusive. This order was determined by the confidence of labeling each feature.

2.2.6. Segmentation evaluation

To assess segmentation quality, we drew CEVs and FHVs manually for 2 sets of 15 subjects selected randomly from the available pool downloaded from the TCIA. These volumes were completed by 2 independent trained operators under the supervision of a neuroradiologist (N.F.) and a neurosurgeon (C.C.C.). Manual delineation of tumor-associated volumes was performed by using the software program AMIRA (http://www.vsg3d.com/amira/overview), using threshold-assisted segmentation on whole-brain T1wCE and FLAIR images that were registered to the Montreal Neurological Institute template. Operator-derived volumes were compared with IPVL-derived volumes by using the Dice similarity coefficient (DICE). This coefficient assesses the similarity between 2 volumes by dividing twice the sum of the intersection by the sum of both volumes [37]. Interoperator similarity was also compared by using this metric. A DICE equal to 1 would imply perfect similarity and overlap of 2 volumes.

2.2.7. Minimum image requirement for adequate segmentation

To assess the performance of our method when fewer imaging sequences were available for input, we implemented IPVL on a group of 15 subjects multiple times while removing ≥1 image, recapitulating common image combinations seen within the TCIA subjects. The segmentations that resulted from these image combinations were compared with operator volumes to determine their DICE similarities. FHVs were not segmented in image combinations that lacked FLAIR sequences.

2.3. Results

2.3.1. Overview of automated segmentation algorithm

The steps of our segmentation protocol, applied to a representative case, are illustrated in Fig 2.1. Generally, our segmentation work flow was divided into 5 stages: preprocessing, preliminary segmentation, classification, probability labeling, and final segmentation. In preprocessing, images were loaded. Bias field correction, skull stripping, and registration to the template were then performed. The results of preprocessing created images in standard space to provide input for preliminary segmentation. Preliminary segmentation assigned voxel labels to CEV, FHV, BV, CSF, GM, WM, and unassigned (for voxels with ambiguous membership) by using k-means-based tissue segmentation and a region-growing algorithm. During classification, voxels sampled from these preliminary labels were used to train the GMM and KNN classifiers. All voxels were then classified to independent labels to identify CEV, FHV, BV, CSF, GM, and WM volumes. During probability labeling, each voxel was assigned a probability of membership to each tissue label. In the last step, final segmentation, voxels were labeled according to their greatest probability, and a voxel continuity filter was applied to eliminate clusters of <150 continuous voxels. The average time required to complete segmentation was 11.12 ± 5.63 minutes.

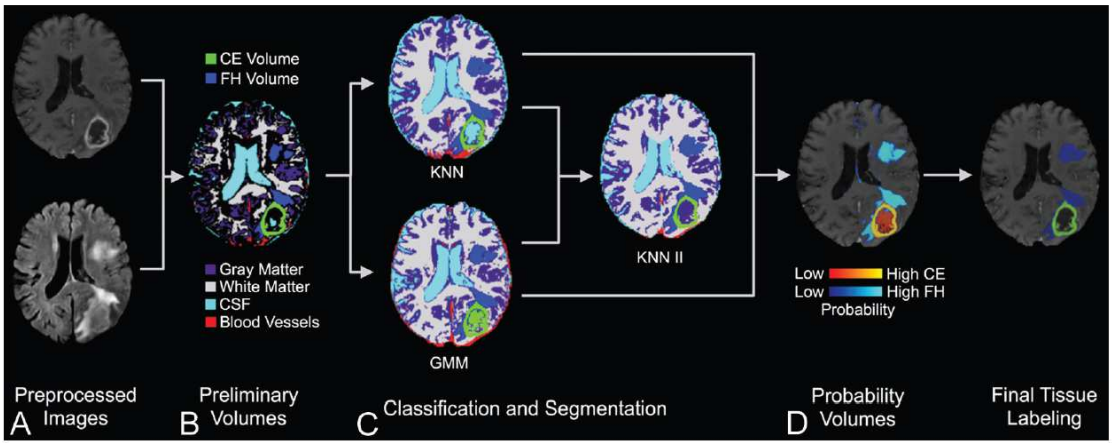

Figure 2.1. Work flow for Iterative Probabilistic Voxel Labeling (IPVL). (A) Downloaded TCIA images were preprocessed. (B) Preliminary segmentation was performed to generate conservative yet highly specific preliminary volumes. (C) In the classification step, these volumes were used to train the GMM and KNN probabilistic classifiers. The consensus of KNN and GMM classification was resampled and used to train a new classifier (KNN II), which assigned voxel tissue labels. The classifiers integrated their respective outputs to generate tissue-specific probability volumes. (D) The voxels were assigned based on their greatest probability of membership to a tissue label, and a voxel continuity filter was applied to eliminate clusters less than 150 continuous voxels.

.

2.3.2. Manual segmentation comparison

Examples from 4 subjects that represented the CEVs and FHVs with the highest and lowest DICE scores relative to operator 1 are shown in Fig 2.2. Corresponding FHV segmentations for CEV and CEV segmentations for FHV are included to show that segmentation success for 1 feature is not necessarily correlated with segmentation success for corresponding features. Analysis showed no statistical difference among operator-derived volumes, so operator 1 was selected as the basis for image comparison (P = .72 for CEV interoperator, and P = .39 for FHV interoperator). Figure 2.2 demonstrates that the algorithm generates highly analogous CEVs and FHVs relative to those derived manually.

IPVL CEVs were statistically indistinguishable from volumes generated by expert operators across all subjects (P = .93). DICE scores, for automated CEVs, relative to operators 1 and 2, averaged 0.923 and 0.921, respectively. These DICE scores were highly comparable with those obtained from interoperator analysis (average of 0.923, Fig 2.3A). For automated FHVs, the DICE scores relative to operators 1 and 2 averaged 0.851 and 0.827, respectively. DICE scores obtained from interoperator analysis averaged 0.905 (Fig 2.3B). Analysis revealed that FHVs were slightly lower than interoperator comparison (P = .04). We observed that FHV DICE scores were poorer than CEV DICE scores for both the interoperator and the operator algorithm comparisons. Overall, the DICE scores for both CEV and FHV

achieved through our algorithm were improved or similar relative to those previously reported [19-25].

To ensure that these results were generalizable, we randomly selected 15 additional subjects for analysis. The results from this analysis are highly comparable with those reported above. DICE scores for automated CEVs relative to operators 1 and 2 averaged 0.921 and 0.901, respectively. These DICE scores were highly comparable with those obtained from interoperator analysis (DICE = 0.905). For automated FHVs, the DICE scores relative to operators 1 and 2 averaged 0.846 and 0.823, respectively. DICE scores obtained from interoperator analysis averaged 0.812.

It was possible that difficult cases, including tumors with multifocal patterns, or tumors with attachment to large vessels or the brain surface, may cause errors in automatic segmentation. Of the images analyzed, 2 glioblastomas (The Cancer Genome Atlas [TCGA]-06–0139, TCGA-06–0166) were multifocal. For these subjects, IPVL-defined CEV and FHV showed mean DICE scores of 0.94 (range, 0.92– 0.95) and 0.92 (range, 0.91– 0.93) relative to expert defined volumes, respectively. Seven tumors (TCGA-02–0048, TCGA-06– 0164, TCGA-08– 0358, TCGA-76– 6280, TCGA-76–6192, TCGA-76–5386, and HF1139) were located on the surface of the cerebrum. For these tumors, IPVL-defined CEV and FHV showed mean DICE scores of 0.92 (range, 0.84–0.96) and 0.84 (range, 0.70–0.95). One tumor (TCGA-76–5385) was attached to a major vessel (the MCA). For this tumor, IPVL-defined CEV and FHV showed mean DICE scores of 0.90 (range, 0.89–0.91) and 0.72

(range, 0.70–0.75). These results suggest that our algorithm performs adequately in anatomic locations and in difficult cases that are historically challenging to previously published algorithms.

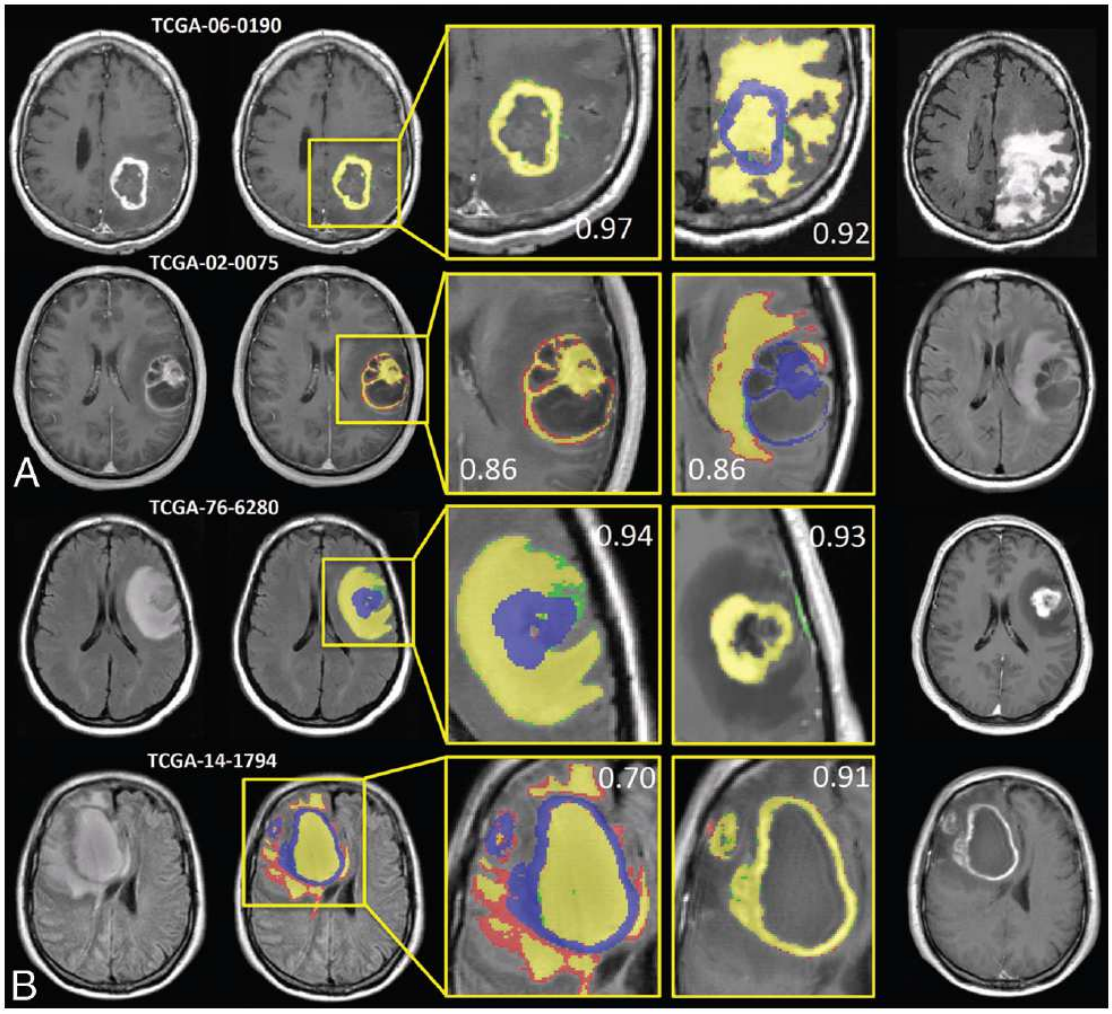

Figure 2.2. IPVL segments volumes that are highly analogous to operator-defined volumes. Results from 4 subjects representing the highest and lowest Dice similarity coefficient (DICE) scores for CEV and FHV segmentations are shown. (A) The highest DICE (top) and lowest DICE (bottom) examples of IPVL-segmented CEVs relative to operator-defined volumes are shown. The corresponding FHV segmentation results are shown (right) to demonstrate that CEV segmentations are independent of FHV segmentations. (B) The highest DICE (top) and lowest DICE (bottom) examples of IPVL-segmented FHV segmentations relative to operator-defined volumes are shown. The corresponding CEV segmentation results are shown as well (right) to demonstrate that FHV segmentations are independent of CEV segmentations. Yellow indicates regions of intersection between operator and IPVL-defined volumes; red: operator-defined volume only; green, IPVL-defined volume only. Corresponding CEV segmentations are overlaid in blue on FLAIR images for clarity.

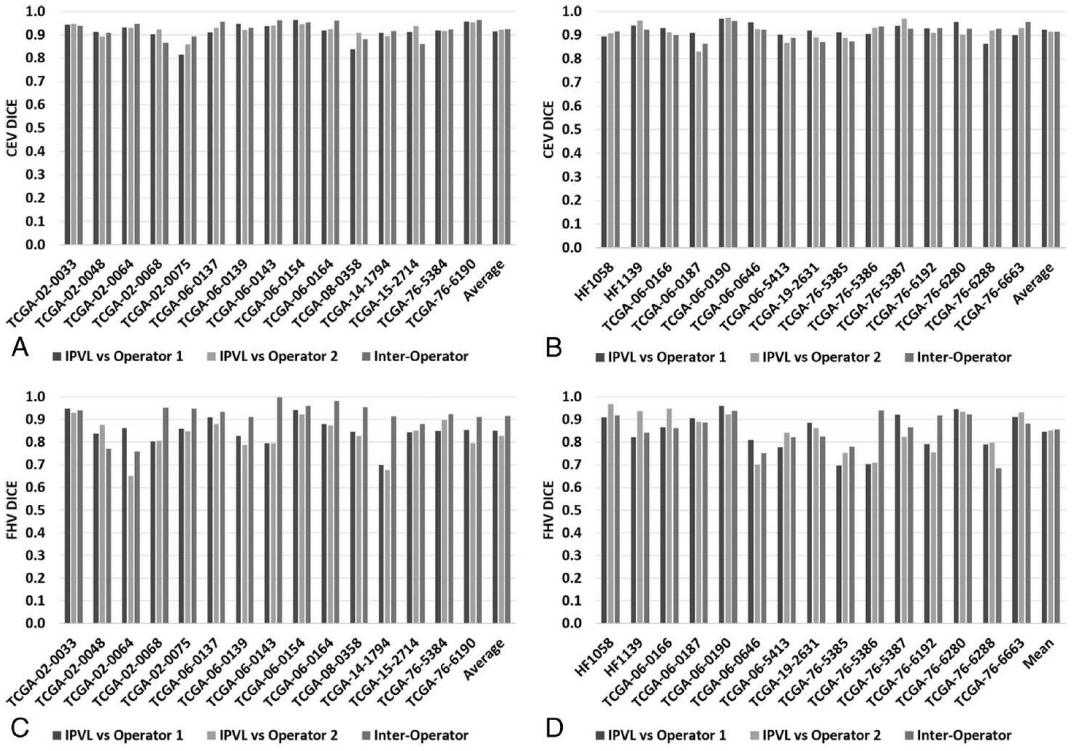

Figure 2.3. Quantitative comparison between IPVL-defined volumes and operator-derived volumes compared with interoperator comparisons. (A and B) DICE comparisons for 2 sets of IPVL-defined and operator-defined CEVs are shown. DICE scores were calculated comparing CEVs generated by IPVL, operator 1, and operator 2. (C and D) DICE score comparisons for IPVL-defined and operator-defined FHVs. DICE scores were calculated comparing FHVs generated by IPVL, operator 1, and operator 2.

2.3.3. Minimal image requirement for adequate segmentation

The TCIA and other image databases include many subjects who do not have the full complement of T1WI, T1wCE, T2WI, and FLAIR images. In the TCIA, this full set of imaging was available in only 52% of subjects. Therefore, it was of interest to determine how our algorithm would perform when limited imaging modalities were available. To this end, we examined how the sequential removal of the various image sequences impacted segmentation performance. DICE scores were determined for a subject's segmentations by using each combination of images relative to operator-defined volumes. These DICE scores were plotted compared with the DICE scores derived from segmentations by using all 4 imaging sequences.

For CEV segmentations, removal of T1WI and T2WI did not significantly affect performance. The DICE scores obtained when comparing volumes delineated by using only T1wCE and FLAIR were comparable with those obtained when all 4 imaging sequences were processed by our algorithm (Fig 2.4A). Similarly, FHV segmentations were minimally impacted by image reduction, and DICE scores by using all 4 imaging sequences were comparable with those obtained when using only T1wCE and FLAIR (Fig 2.4B).

To further characterize the impact of reducing the number of image sequences on the performance of CEV and FHV segmentations, we also plotted the range of DICE scores that resulted from removing ≥1 image series for each subject. For most subjects, removing images minimally impacted

DICE scores—that is, the segmentation quality was not significantly altered (Fig 2.4C for CEV, Fig 2.4D for FHV). For FHV segmentations, removal of T2WI and T1WI did not significantly alter segmentation performance (Fig 2.4D for FHV).

Only 2 subjects, TCGA-02–0068 and TCGA-06–0164, had increased vessel contamination of the CEVs when FLAIR images were removed during image-reduction analysis. CEV segmentations for image combinations that contained at least a FLAIR and T1wCE image were highly comparable across all subjects (Fig 2.4E). While adequate CEV segmentation required only T1wCE for most cases, FLAIR images improved CEV and BV discrimination and may be required for segmentation in a subset of subjects. Most surprising, CEV segmentation for T1wCE and FLAIR alone was nearly identical to CEV segmentation results that used all available imaging series. These results suggest that our algorithm requires only T1wCE and FLAIR images for robust volume segmentation of both tumor-associated CEVs and FHVs.

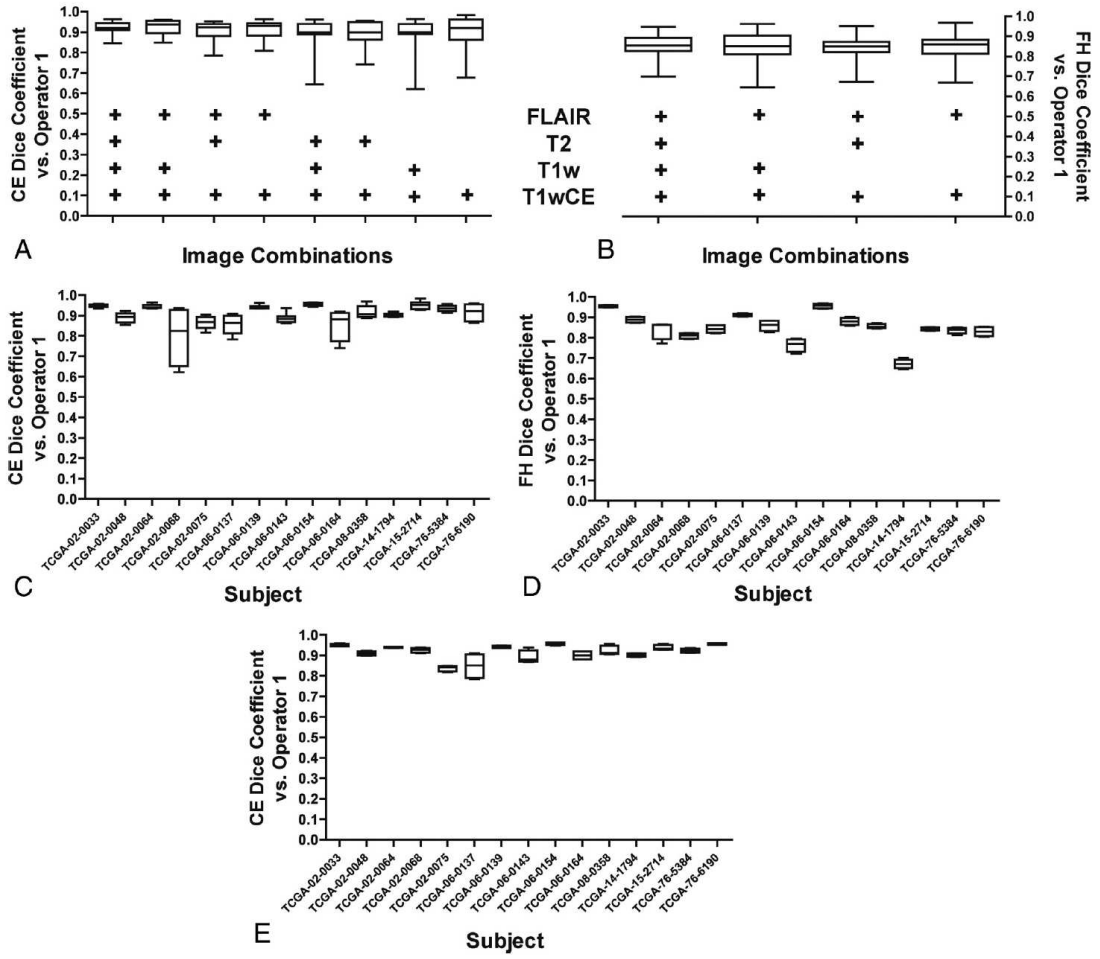

Figure 2.4. Effects of removing image sequences on IPVL segmentation. (A) Select image sequences (such as T1WI) were removed before IPVL CEV segmentations for each subject. The image sequences that were available during IPVL segmentation are indicated by a plus sign. DICE scores were calculated for the resultant CEVs relative to operator 1–defined CEVs. The distribution of DICE scores across all subjects because of image sequence removal is shown as a boxplot. (B) Select image sequences were removed before IPVL FHV segmentations. DICE scores were calculated for the resultant FHV segmentations relative to operator 1–defined FHVs. The distribution of DICE scores across all subjects due to image sequence removal is shown as a boxplot. (C) A boxplot demonstrates the range of DICE scores for IPVL-segmented CEVs relative to operator defined CEVs per patient for all image combinations tested. (D) A boxplot demonstrates the range of DICE scores for IPVL-segmented FHVs relative to operator-defined FHVs per patient for all image combinations tested. (E) A boxplot demonstrates the range of DICE scores for IPVL-segmented CEVs relative to operator-defined CEVs per patient when only T1WI and FLAIR source images were used for IPVL segmentation.

2.4. Discussion

The success of any automated segmentation process hinges on the a priori definition of the features that constitute a volume of interest. Human vision can integrate visual data along with both experience and assumption to distinguish and classify independent features. This task is often challenging for a computer because the cross-section of data available to the computer is often simplified. We hypothesized that the complexity of image segmentation could be largely recapitulated by using iterating probabilistic classifiers trained on sparse subject-specific preliminary features. To test this hypothesis, we predefined the voxels that were most likely associated with the features of interest to generate preliminary volumes. We then used k-nearest neighbor and GMM probabilistic classifiers to refine the segmentation process. In our algorithm, these complementary probabilistic classifiers were integrated in an iterative manner to converge on a segmentation result for the various features of an MR image. Our results demonstrate that IPVL image segmentation is highly comparable with segmentations that were drawn manually.

Most important, the time required for segmentation per subject averaged 11.2 minutes when all 4 image sequences were used. In contrast, manual segmentation by experts required 1–3 hours depending on the size and complexity of the volume to be segmented. As such, our method presents an opportunity for high-throughput quantitative analysis of TCIA images and other imaging databases. The insensitivity of our algorithm to interinstitutional

methodologic differences in MR imaging supports its utility for this application. Further supporting the utility of our algorithm, we demonstrated that only 2 image sequences (the T1wCE and FLAIR images) are needed for reliable segmentation of tumor CEVs and FHVs. Finally, using a common template space will provide a platform for future analyses, intersubject comparisons, and longitudinal studies.

While our study was focused on the development of an algorithm for research use in terms of radiographic biomarker discovery, reliable volume segmentation by using our algorithm may also impact clinical practice. For example, it is often difficult to detect subtle differences in the radiographic appearance of a tumor during disease progression. As a result, changes in serial MR imaging may be underappreciated until a patient becomes symptomatic. Automated segmentation and longitudinal quantitative comparison may help facilitate the detection of subtle radiographic changes, such as tumor progression, thereby allowing clinicians to perform procedures to prevent clinical deterioration in select patients. Application of these methods may also aid the evaluation of the therapeutic response in clinical trials.

Careful study of the discrepancies between the volumes generated by IPVL and expert-defined volumes revealed a few limitations. The algorithm can fail to detect tumor contrast enhancement or FLAIR hyperintensity in regions of these volumes that fall below a single voxel (~1 mm). This limitation, a result of voxel sampling and partial volume effect, could be mitigated with higher resolution imaging. In a few subjects (eg, TCGA-02–

0068, TCGA-06–0154), reliable delineation of BV volume from tumor CEVs remained challenging when image combinations lacking FLAIR images were used for segmentation, leading us to conclude that FLAIR and T1wCE are required for our method. Segmentation of FLAIR volumes remains a challenge, but this challenge is shared by the human eye as demonstrated by the interobserver discrepancies reported previously. The use of higher order image processing, such as textural analysis, may facilitate the improvement of our algorithm in the near future.

2.5. Conclusions

We demonstrate that iterative probabilistic voxel labeling is a reliable and robust tool for automatic segmentation of MR images in the TCIA dataset. Application of this method could facilitate quantitative radiographic assessment of glioblastoma for both researchers and clinicians alike.

Chapter 2, in its entirety, has been accepted by the American Journal of Neuroradiology for publication. Tyler C. Steed, Jeffrey M. Treiber, Kunal S. Patel, Zach Taich, Nate S. White, Michelle L. Treiber, Nikdokht Farid, Bob S. Carter, Anders M. Dale, Clark C. Chen. "Iterative probabilistic voxel labeling (IPVL): automated segmentation for analysis of The Cancer Imaging Archive (TCIA) glioblastoma images." The dissertation author is the primary investigator and author of the manuscript.

3. Differential localization of glioblastoma subtype implicates the sub-ventricular zone (SVZ) in glioblastoma pathogenesis

The subventricular zone (SVZ) has been implicated in the pathogenesis of the molecularly diverse neoplasm, glioblastoma. Whether molecular subtypes arise from unique niches of the brain remains largely unknown. Here, we tested whether these subtypes of glioblastoma occupy distinct regions of the cerebrum and examined glioblastoma localization in relation to the SVZ.

Pre-operative MR images from 217 glioblastoma patients from The Cancer Imaging Archive were segmented automatically into contrast enhancing (CE) tumor volumes using Iterative Probabilistic Voxel Labeling (IPVL). Tumors were subtyped as either the glioma-CpG island methylator phenotype (G-CIMP), proneural, neural, classical, or mesenchymal subtypes using published methods. Probabilistic maps of tumor location were generated for each and compared quantitatively. Distances were calculated from the centroid of CE tumor volumes to the SVZ and correlated patient survival and gene expression.

Across all patients, CE tumor volumes were observed at a higher density near the SVZ. Proneural and neural glioblastomas were more likely to be located in the left temporal lobe and be in closer proximity to the SVZ. Classical and mesenchymal glioblastomas were more diffusely distributed and

located farther from the SVZ. Irrespective of subtype, proximity to the SVZ was associated with poorer overall survival (p = 0.001), expression of the stem cell marker CD133 (p = 0.006), and a published HOX-associated glioblastoma stem cell signature (p=0.030). Glioblastoma subtypes occupy different regions of the brain and vary in proximity to the SVZ. These findings harbor implications pertaining to the pathogenesis of glioblastoma subtypes.

3.1. Introduction

Glioblastoma remains one of the deadliest of human cancers [2]. One challenge to meaningful therapeutic development is glioblastoma's inter-tumoral heterogeneity. Large-scale genomic analyses of clinical glioblastoma samples have identified at least five distinct subtypes of glioblastoma, with distinct biologic and clinical behaviors [5, 8, 38, 39]. These subtypes include classical, mesenchymal, neural, proneural, and the glioma-CpG island methylator phenotype (G-CIMP). It remains unclear whether these molecular differences arise as a result of distinct cells of origin, genetic/epigenetic landscape, mutation spectrum, or microenvironment.

The sub-ventricular zone (SVZ), which lies adjacent to the lateral wall of the lateral ventricle, is a site where neural stem cells (NSC) and astrocyte precursors are located in the adult brain [40-42]. During neural development, NSCs migrate radially and differentiate into various progenitor cells during this process [43-45]. Studies suggest that SVZ NSCs and astrocyte precursors may give rise to subsets of glioblastomas which demonstrate distinct physiological behavior [46, 47]. It is known that many primary CNS neoplasms, including IDH1 mutant glioma, occur in regions corresponding to distinct cells of origin [48-50]. We hypothesize that glioblastoma tumor location as a function distance from the SVZ may be indicative of its cell of origin and distinct molecular physiology.

Using Iterative Probabilistic Voxel Labeling (IPVL) [51] , a method of automatic tumor segmentation developed by our laboratory, and imaging data obtained through The Cancer Imaging Archive (TCIA), we quantitatively determined the geographic distribution for each of the molecular glioblastoma subtypes and quantified each tumor's distance to the SVZ. Our analysis indicates that proximity to SVZ is associated with poor overall patient survival, and gene expression associated with glioma stem cell biology.

3.2. Materials and Methods

3.2.1. Data acquisition and Subtype Classification

We searched the TCIA for subjects with at least one artifact-free pre-operative T1 weighted MR image with contrast. In total, 217 subjects with MR images were downloaded from the TCIA (http://cancerimagingarchive.net) in November 2014. Level 3 probe collapsed Messenger RNA (mRNA) expression data: Affymetrix HT-HG-U133A GeneChip and RNAseq, was downloaded for available patients via the TCGA Data Portal (http://tcga-data.nci.nih.gov/tcga/). Affymetrix expression data were normalized by robust multichip average (RMA) [52]. RNAseq data were RSEM normalized [53]. When not already available in published literature, genomic subtypes were determined for subjects employing single sample Gene Set Enrichment Analysis (ssGSEA) as described previously [8, 54]. Additionally, G-CIMP status was determined using methods described previously [5, 8].

3.2.2. Image Preprocessing and Registration

MR images were corrected for gradient nonlinearity using previously described methods [27, 55]. Images were additionally preprocessed and intensity corrected utilizing N4 bias field correction [56], then affine and nonlinear registrations were performed to the Montreal Neurological Institute (MNI) 152 nonlinear 1 mm^3 template employing methods from Advanced Normalization Tools (ANTS) [57]. Visual inspection of resulting images was

performed by three independent reviewers (T.C.S, J.M.T, & K.S.P) to ensure successful and accurate preprocessing was completed for all subjects.

3.2.3. Tumor Segmentation and Probability Maps

Contrasting-enhancing (CE) regions of tumors were segmented using the iterative probabilistic voxel labeling (IPVL) algorithm developed in the laboratory [51] (Figure 3.1B) and the enclosed volume was filled using a 3D morphological open-close operation (Figure 3.1C). Tumor density maps were calculated as the number of observations at each voxel divided by the number of subjects (Figure 3.1E). Similarly, centroid density maps were generated using a 15-mm centroid of each filled CE volume (Figure 3.1D). Visual inspection by two independent operators (T.C.S, J.M.T) was performed to ensure adequacy of region filling and centroid estimation. Probability distributions were quantitatively compared using a voxel-wise two-tailed Fisher's exact test [58] comparing the number of tumors observed for each subtype at each voxel. Only significant clusters which had a > 5% probability of occurring by chance were kept.

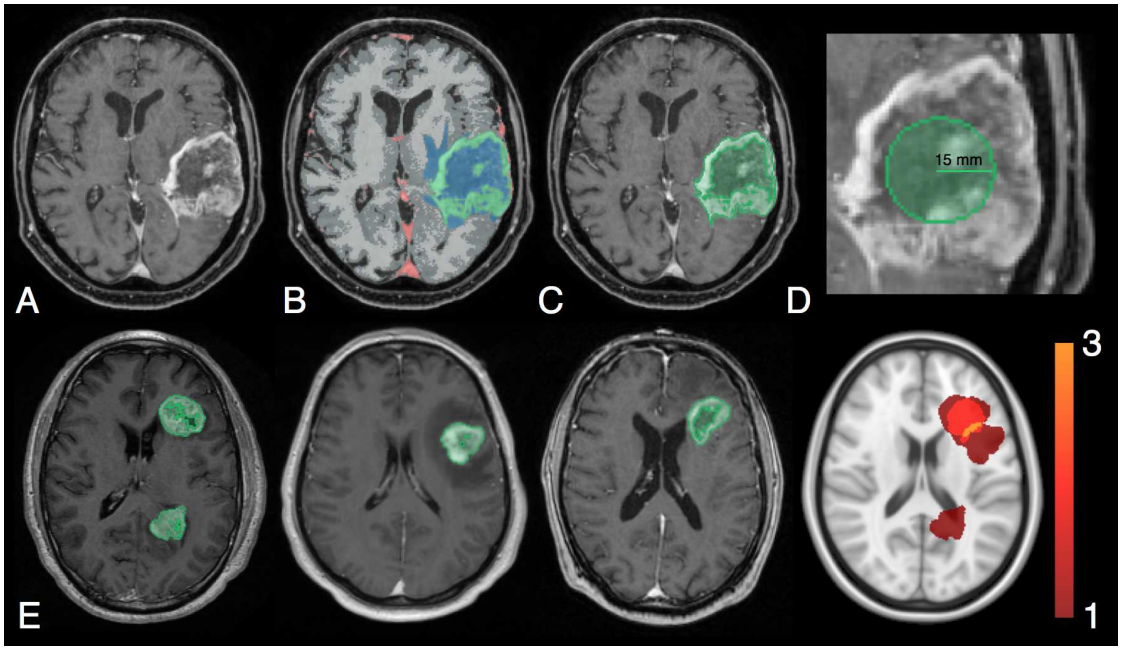

Figure 3.1. Workflow for generation of total CE and centroid density maps. Preprocessed images (A) were registered to the Montreal Neurological Institute (MNI) template and segmented according to the IPVL pipeline (B). CE volumes were filled (C) and centroid of each were calculated (D). Filled CE volumes from each subject were summed (E) and then converted to probabilities by dividing by the total number of subjects.

3.2.4. Subventricular Zone Distance

To measure SVZ distance with respect to each tumor's filled CE volume, the MNI template's lateral ventricle segmentation was used as a basis of comparison. SVZ distances were calculated by taking the mean of the distance from the nearest MNI template ventricular border to each point within a subject's CE volume. Statistical analyses of SVZ distance with respect to patient survival was performed within the statistics software package SPSS (IBM Corp, New York, United States). When stratification was required, tumors were classified by the median of the SVZ distance: low SVZ (SVZ distance < 19.23 mm) and high SVZ (SVZ distance $\geq$ 19.23 mm).

3.2.5. ssGSEA and Statistical Analyses

ssGSEA was employed to calculate normalized enrichment scores for gene signatures according to established methods [54], using custom software in MATLAB (Statistics Toolbox Release 2012b, The MathWorks Inc., Natick, MA) [59]. Statistical analysis of SVZ distance and gene expression was performed in MATLAB. All mRNA expression analyses were performed in the Affymetrix HT-HG-U133A RMA normalized data. A one-tailed t-test was performed to determine whether low SVZ score is associated with increased mRNA expression. To mitigate for type I error, during hypothesis testing 100,000 permutation test were performed in our sample to determine the likelihood of the outcome measured occurring by chance.

3.3. Results

3.3.1. Glioblastoma Density Map

The workflow for CE segmentation and CE centroid placement is described in Methods and shown in Figure 1. Information regarding patient demographics, patient survival, and tumor CE volumes for each patient are available in Table 3.1. The filled CE volume from all subjects are layered and generated in template space yielding a glioblastoma density map and shown as Figure 3.2. The centroid of CE volume for each patient was similarly layered to create a density map, which confirmed the same distribution. The overall glioblastoma density map reveals a strong predilection for tumors to occur within the periventricular white matter near the SVZ. High tumor densities occur adjacent to the temporal horn and atria, bilaterally. The highest probability region was observed near the right atrium MNI coordinate (35, -40, 6), an 18% probability. Tumor densities are enriched around the SVZ which is demonstrated by the fact that 25.7% of all CE volume probabilities were found within 10 mm of the ventricular volume, a region representing only 12.6% percent of the total brain volume. Our findings concerning global glioblastoma distribution are consistent with previous imaging based reports of glioblastoma in independent cohorts [55, 60].

Table 3.1. Summary of demographic data, clinical outcome, and radiographic CE volume.

Table 1: Demographic data							
Variable	All	G-CIMP+ Proneural	G-CIMP- Proneural	Neural	Classical	Mesenchymal	Unknown
N (%)	217 (100)	10 (4.6)	46 (21.2)	39 (18.0)	51 (23.5)	57 (26.3)	14 (6.5)
Male, No. (%)	128 (59.8)	6 (66.7)	25 (55.6)	25 (64.1)	23 (45.1)	39 (68.4)	10 (76.9)
Female, No. (%)	86 (40.2)	3 (33.3)	20 (44.4)	14 (35.9)	28 (54.9)	18 (31.6)	3 (23.1)
Age, y, mean ± SD	59.3 ± 14.1	41.5 ± 15.4	57.9 ± 15.1	62.0 ± 13.3	61.2 ± 15.0	60.7 ± 11.2	56.6 ± 12.0
KPS, mean ± SD	77.9 ± 14.1	86.7 ± 10.0	76.6 ± 9.9	78.2 ± 19.3	75.0 ± 14.3	79.6 ± 13.4	75.5 ± 16.3
OS, d, mean ± SD	405.8 ± 336.0	680.8 ± 287.1	320.4 ± 343.2	427.8 ± 300.9	433.6 ± 291.8	429.0 ± 388.2	197.0 ± 159.5
PFS, d, mean ± SD	261.2 ± 271.8	441.6 ± 593.0	241.9 ± 315.9	255.2 ± 189.2	241.0 ± 169.2	294.1 ± 308.3	151.5 ± 118.2
CE volume, voxels, mean ± SD	34977 ± 33406	26809 ± 12454	29015 ± 18364	40504 ± 37324	32496 ± 20217	39371 ± 49242	35146 ± 25987

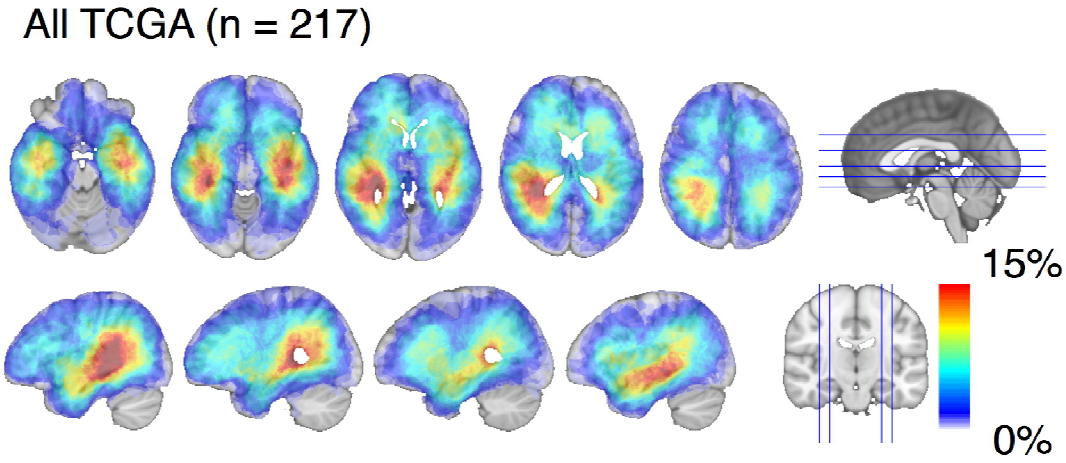

Figure 3.2. Radiographic glioblastoma density map. Total CE probability map revealed that glioblastoma, as a whole, exhibit a strong predilection occurrence in proximity to the SVZ. Red indicates the highest frequency of overlap and light-blue indicating the lowest frequency of overlap.

3.3.2. Glioblastoma Subtype Specific Density Maps

We next generated CE density maps for each glioblastoma subtype. Using these maps, we observed that proneural and neural tumors tend to occur in the temporal and frontal lobe. Both of these subtypes demonstrated a predilection towards asymmetry, having higher densities in the left temporal region relative to the right (Figure 3.3). Conversely, the classical and mesenchymal subtypes were more diffusely distributed in the cerebrum, with significantly lower probabilities of overlap ($p < 0.001$) (Figure 3.3). The classical subtype had higher probability densities within the periventricular white matter adjacent to the right atrium. Statistical comparisons between the probability density maps for all subtypes using voxel-wise Fisher's exact testing (see Methods) confirmed the distributions described above demonstrating regions that are highly specific for each subtype. The statistically significant regions associated with each subtype are demonstrated by Figure 3.4.

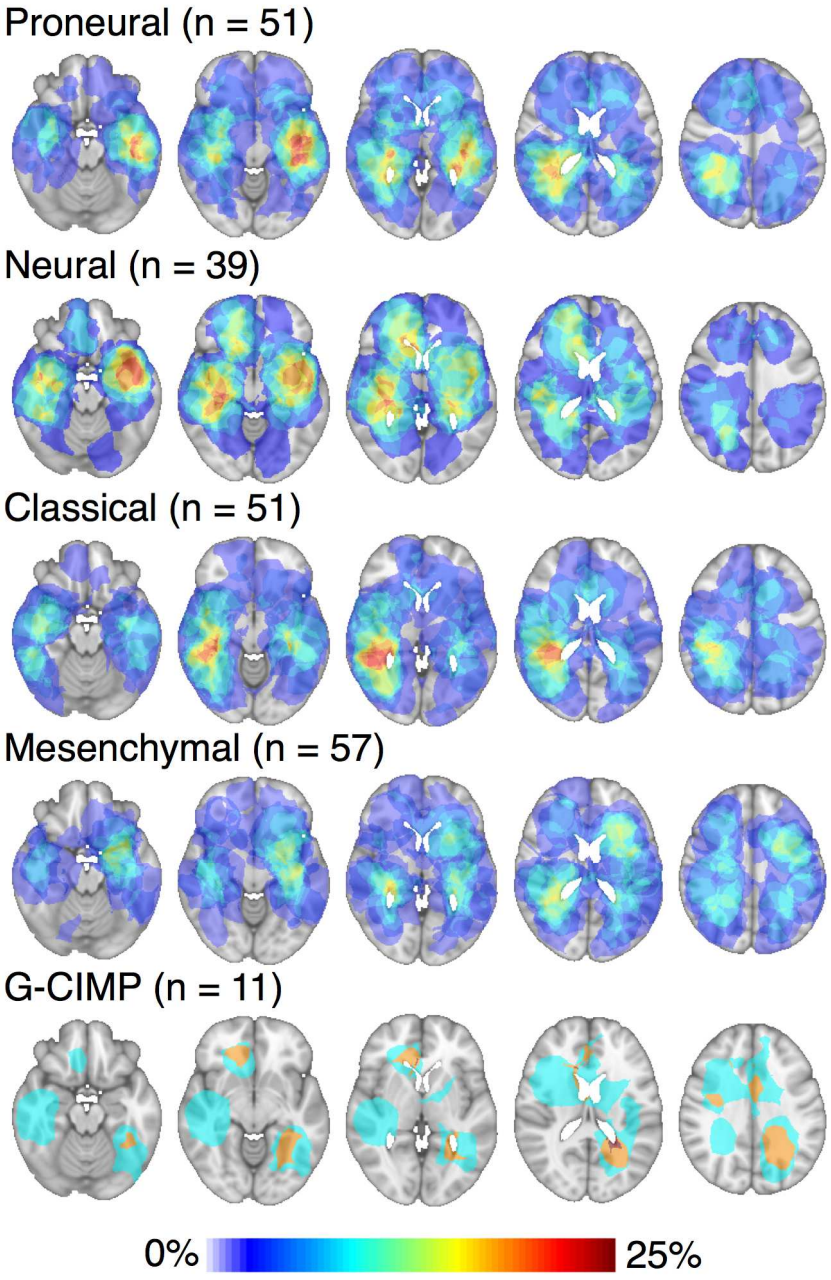

Figure 3.3. Glioblastoma subtype density maps. Subtype-specific density maps were generated using total CE volume. Red indicates the highest frequency of overlap and light-blue indicating the lowest frequency of overlap.

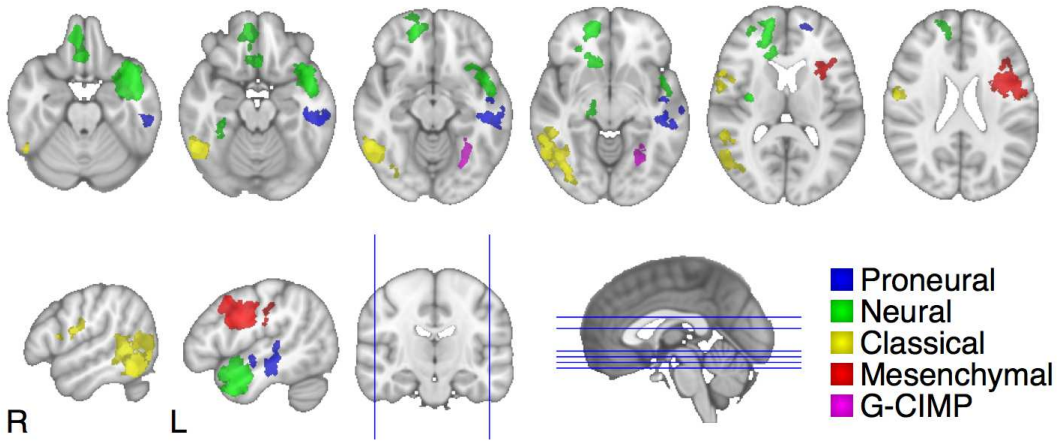

Figure 3.4. Regions of statistically significant subtype localization. Axial (first row) and sagittal (second row) of statistically significant clusters ($p < 0.05$) by subtype. Statistical comparisons were carried out using voxel-wise Fisher's exact tests.

3.3.3. The SVZ Distance

An illustrative example of the SVZ distance measure is demonstrated in Figure 3.5A. The proneural subtype had the lowest mean SVZ distance of all molecular subtypes (p = 0.022). Furthermore, there was a statistical difference between the combined proneural and neural subtypes against the mesenchymal and classical subtypes (p = 0.035) (Figure 3.5B). There was no statistical difference when comparing the classical subtype to the mesenchymal subtype. Across all patients decreased tumor SVZ distance was strongly associated with decreased patient overall survival even when correcting for the known survival associated variables; patient age and Karnofsky Performance Score (KPS) (Figure 3.5C) (Cox p=0.001, log rank p=0.002). A Cox regression table demonstrating survival associations with the SVZ distance is shown in Figure 3.5D. This effect was more pronounced for the mesenchymal/classical glioblastoma subtype relative to the proneural and neural subtypes.

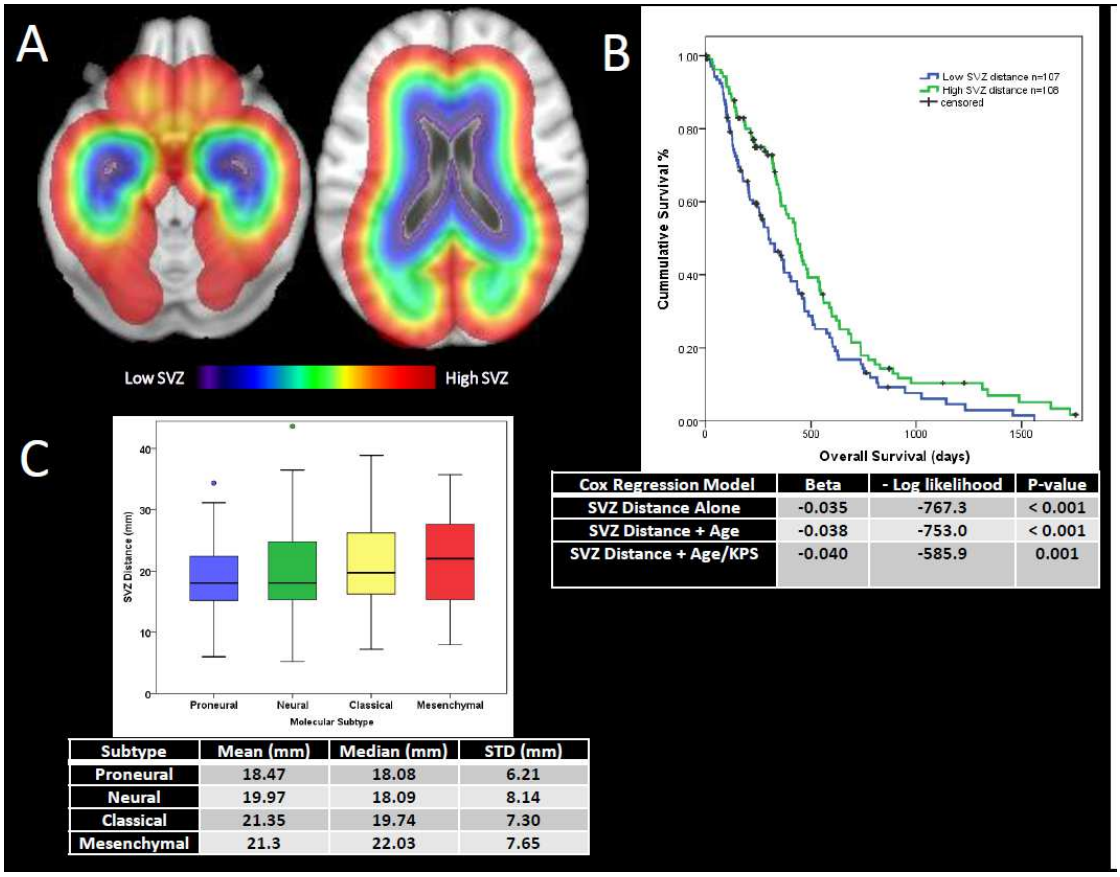

Cox Regression Model	Beta	- Log likelihood	P-value
SVZ Distance Alone	-0.035	-767.3	< 0.001
SVZ Distance + Age	-0.038	-753.0	< 0.001
SVZ Distance + Age/KPS	-0.040	-585.9	0.001

Subtype	Mean (mm)	Median (mm)	STD (mm)
Proneural	18.47	18.08	6.21
Neural	19.97	18.09	8.14
Classical	21.35	19.74	7.30
Mesenchymal	21.3	22.03	7.65

Figure 3.5. Association of SVZ distance with overall survival and CD133 gene expression. (A) Graphical illustration of the SVZ distance measurement. SVZ distance is color coded so that blue indicates shorter SVZ distances while red indicates high SVZ distances. (B) Kaplan Meier Survival curve demonstrating association of lower SVZ distance and reduced overall survival for all glioblastomas (n=217). Below: Cox table demonstrating association of SVZ distance and overall survival for glioblastoma subtypes with correction for patient age and Karnofsky Performance Score (KPS). (C) Boxplot and table of SVZ distances stratified by subtype. Proneural/neural glioblastoma subtypes exhibit shorter SVZ distance relative to mesenchymal/classical subtypes.

3.3.4. SVZ Distance and Glioblastoma Biology

We had hypothesized that glioblastomas arising in proximity to the SVZ may arise from NSCs and glial precursors that are known to reside in this region [44, 61]. A corollary of this hypothesis is that proximity to SVZ should identify with gene expression patterns that recapitulate stem-like cell derivation. CD133 is a glycoprotein expressed in neuronal and glial stem cells that reside in the SVZ [46, 62]. It is also known that some brain tumors exhibit expression of CD133 [62]. We therefore tested whether glioblastoma CD133 expression correlated with SVZ distance. Realizing that the TCIA consists of a single dataset and validation is critical in any form of bio-statistical analysis, we performed our assessment with specific hypotheses in mind. Briefly, each patient's glioblastoma is classified as "high" or "low" for SVZ distance based on the median value of SVZ for the entire cohort. A one-tailed t-test was performed to determine whether low SVZ score was associated with increased CD133 mRNA expression (as determined by the affymetrix HG U133A array) in our dataset. This analysis confirmed that glioblastomas located in proximity to the SVZ harbored a statistically significant increased expression of CD133 ($p = 0.006$).

Recent literature has suggested an important role for HOX gene expression in glioblastoma initiation and chemo and radiotherapy resistance [63, 64]. These genes are important during development, ultimately governing the patterning and mosaicism seen throughout the brain [65]. To further confirm our hypothesis, we tested whether a published HOX signature

associated with glioblastoma “self-renewal” is associated with SVZ distance [64]. Using the above methods, we found that the ssGSEA score for the HOX-associated gene signature correlated with SVZ distance. Specifically, high HOX ssGSEA score was associated with proximity to SVZ ($p=0.03$). Finally, we specifically sought to test the association of HOXA9 with SVZ distance as this gene has been implicated in glioma transformation, therapeutic resistance, and stemness in glioblastoma [64, 65]. Using the method employed for CD133, we found that HOXA9 expression was higher nearer in tumors nearer the SVZ ($p=0.012$). In aggregate, these results suggest that SVZ distance may represent an imaging proxy for the underlying glioblastoma biology.

3.3. Discussion

Tumor density mapping of glioblastoma images derived from 217 TCIA patients demonstrated that the CE-defined glioblastoma volumes are densely concentrated near the SVZ, which recapitulates the global distribution of glioblastomas previously observed in an independent cohort [55, 60]. Our study provides a quantitative tumor density map of glioblastoma subtype and robustly demonstrates that these subtypes occupy distinct regions of the brain using independent imaging methods. Intriguingly, the subtypes exhibit regional associations with regard to the SVZ, an area of critical importance in neurogenesis and glioblastoma pathogenesis. The proneural and neural glioblastomas exhibit similar localization and clustered around the SVZ of the left temporal horn. In contrast, the classical and mesenchymal glioblastomas exhibit a more diffuse distribution and tend to localize farther from the SVZ. These pattern localizations are somewhat reminiscent of the maturation of NSCs during development. In this process, stem cells migrate radially from the SVZ to the cortical surface and become differentiated progenitor cells. In this context, it is possible that the localization of glioblastoma subtypes reflect their cell of origin in NSC progenitor cells.

The asymmetric distribution of proneural and neural subtypes presents an unexpected phenomenon. A large body of work has documented asymmetry in cerebral function and activity [66], with inferred asymmetry in terms of anatomic substrate and physiologic circuit [67-69]. It is possible that

molecular microenvironment or differential cell-related asymmetry contributes to glioblastoma pathogenesis. For instance, recent studies suggest that many neurotransmitters serve as trophic factors that mediate mitogenic signaling in glioblastomas [70]. Increased utilization of such neurotransmitters, or differential levels of adult neurogenesis may effect regional predisposition for glioblastoma pathogenesis. Furthermore, patients with tumors affecting the left temporal lobe may present with symptoms earlier, potentially increasing their likelihood for detection and enrollment in the TCGA.

It is remarkable that, independent of molecular subtype, the proximity of a glioblastoma to the SVZ is associated with genomic and clinical differences. From a genomic perspective, proximity to the SVZ is associated with increased expression of CD133 as well as a HOX signature. From a clinical perspective, proximity to the SVZ is associated with decreased overall survival. While we cannot exclude the possibility that the survival differences may be related to the morbidities associated with surgical access of deep lesions [71], the association between SVZ distance, CD133, and the HOX gene signature suggest that the biology of the underlying tumor likely contributed to the difference in survival.

Chief amongst the limitations of our study is the assumption that the center of tumor mass approximates the site of tumor origin. This was assumed as our dataset does not have available prospective imaging. Another challenge encountered during our study involves the deformation of ventricular contour by glioblastoma mass effect. To address this issue, we utilized

established methods of non-linear registration [57] to MNI atlas to account for such deformations. Despite these corrections, distributions of CE tumors volumes derived using these methods largely recapitulated the results from CE volumes derived linearly (data not shown). Finally, while robust statistical analysis is performed in this dataset in a hypothesis-driven manner, further verification of our results is warranted.

3.4. Conclusions

Integration of quantitative MR image analysis of 217 TCIA subjects and molecular subtyping of glioblastoma revealed subtype specific brain localization and differed with regard to the SVZ. Quantitative proximity to the SVZ, as determined by our methods, may be an imaging proxy for the underlying glioblastoma biology.

Chapter 3, in part, is currently in preparation for submission for publication of the material. Tyler C. Steed, Jeffrey M. Treiber, Kunal S. Patel, Bob S. Carter, Anders M. Dale, and Clark C. Chen. Tentatively entitled “Differential localization of glioblastoma subtype implicates the sub-ventricular zone (SVZ) in glioblastoma pathogenesis.” The dissertation/thesis author was the primary investigator and author of this material.

4. Quantification of lateral ventricular displacement magnitude in glioblastoma imaging from the TCIA is associated with patient survival

When brain tumors like glioblastoma arise, tumor mass displaces tissue as a function of neoplastic growth and cerebral compliance. Brain tumors of similar sizes can exert differential mass effect. We defined a novel parameter to quantify this phenomenon and serve as a proxy measurement for mass effect termed Lateral Ventricle displacement (LVd). Pre-operative MR images from 194 glioblastoma patients from The Cancer Imaging Archive (TCIA) were automatically segmented using our previously reported algorithm termed Iterative Probabilistic Voxel Labeling (IPVL). The distance between center of mass of the tumor patients lateral ventricles and the normal template's lateral ventricles was quantified and termed LVd. Survival and genomic associations with this parameter were investigated using differential gene expression and single sample gene set enrichment analysis (ssGSEA). The variance of LVd was not explained by contrast-enhancing (CE) tumor volume and FLAIR volume alone. This was demonstrated by glioblastomas with similar CE volume, FLAIR volume, and total tumor volume (CE+FLAIR) showing varied LVd values. While CE, FLAIR, and total tumor volume were not associated

with overall survival, higher LVd in pre-operative scans, was associated with poorer survival (p=0.006 Cox regression, age adjusted). Glioblastomas with higher LVd exhibit expression of genes required for aerobic respiration, while tumors with lower LVd had higher expression of genes involved in neural differentiation. This study defines and characterizes a novel quantitative radiographic parameter termed LVd. This noninvasive measure, a proxy for mass effect, associates with poor overall survival and could be used to evaluate patients with glioblastoma.

4.1. Introduction

The Monroe-Kellie doctrine is a fundamental application of physical principals to the dynamics of the cranial compartment. It states that the sum of volumes attributable to CSF, parenchyma, and vasculature must remain constant, and therefore any changes in volume to one compartment must be compensated for proportionally by changes in the others. This doctrine can be applied to brain tumors, like glioblastoma, wherein neoplastic growth displaces tissue resulting in a collapse of CSF volume[72]. This phenomenon has been widely referred to as mass effect. Mass effect is an important factor evaluated during radiographic interpretation of cerebral MR images in a multitude of diseases[73-75]. Mass effect results in increased intracranial pressure leading to brain herniation which, if uncorrected, may prove fatal. Qualitative classification of mass effect has demonstrated prognostic significance in glioblastoma previously[76-78], but concrete definitions and methods of precisely quantifying mass effect for clinical use have not yet been described. Additionally, although it is evident that brain tumors of similar sizes can exert differential mass effects, the physiologic basis for this remains unclear. It is likely that mass effect in brain tumors is attributable to a balance between degree and rate of neoplastic tissue growth[3] and erosion/transformation of surrounding parenchymal tissue.

Here, we propose a novel radiographic parameter entitled Lateral Ventricle displacement (LVd) in an effort to quantify mass effect and better

understand the physiologic basis of this feature in glioblastoma. Applying first principles inspired by the Monroe-Kellie doctrine, this method measures the magnitude of displacement from the lateral ventricular center of mass (CoM) in glioblastoma patients relative to the CoM from a defined “normal” template. This measure accurately and reproducibly quantifies the degree of shift independent of tumor location. Using automatic methods of segmentation developed by our laboratory, LVd defines a new quantitative parameter which strongly associates with reduced survival glioblastoma, yielding new prognostic applications.

4.2. Materials and Methods

4.2.1. Data acquisition and Imaging

Pre-operative MR images from 194 glioblastoma patients from The Cancer Imaging Archive (TCIA) TCGA GBM cohort and 550 non-tumor control subjects from University College in London were registered to a standard template and segmented using our Iterative Probabilistic Voxel Labeling (IPVL) algorithm [51]. MR images were obtained from TCIA (http://cancerimagingarchive.net) in June 2014. Inclusion criteria included patients with at least one artifact free pre-operative T1 weighted MR image with contrast. Patient demographic data is listed in Table 1. Level 3 probe collapsed Messenger RNA (mRNA) expression data (affymetrix HG U133A array) was downloaded for the subset of 165 patients along with Level 3 mRNA Sequencing data for 146 patients via the TCGA Data Portal in June 2014.

4.2.2. Image Preprocessing and Registration

Spatial and intensity distortions caused by nonlinearity warping were corrected using previously described methods[27]. In order to compare tumor localization across subjects, imaging data was registered to the Montreal Neurological Institute (MNI) 152 nonlinear 1 mm^3 template using FSL's linear registration tool[32] with an affine transformation. Visual inspection was

confirmed by three independent reviewers to ensure successful preprocessing for all subjects.

4.2.3. Tumor Segmentation and Probability Maps

Contrasting-enhancing regions of tumors were segmented using a fully automated iterative probabilistic voxel labeling (IPVL) segmentation algorithm developed in the laboratory (Chapter 2, in press, “Iterative Probabilistic Voxel Labeling: Automated Segmentation for Analysis of The Cancer Imaging Archive Glioblastoma Images”, Amer J Neuroradiol). Visual inspection was performed by our independent operators ensuring that segmentation was accurate.

4.2.4. Subventricular Zone Distance

Tumor SVZ distances were measured as described previously. With respect to the tumor segmentation volumes, the template lateral ventricles were segmented and reflected across the midline to yield a symmetric ventricular segmentation. SVZ distances were calculated by taking the mean of the distances from the ventricles at each point contained within a subject’s tumor volume.

4.2.5. Lateral Ventricular Displacement

To calculate lateral ventricular displacement two procedures were utilized during image segmentation. Non-linear diffeomorphic registration was performed using Advanced Normalization Tools ANTS to define a warp field to

apply to the lateral ventricular segmentation [57]. Lateral ventricular segmentation was masked to exclude regions of tumor pathology. The distance between the CoM of subject's lateral ventricles and the template's lateral ventricle CoM was measured. An illustrative example of LVd derivation for an example subject is shown in Figure 4.1.

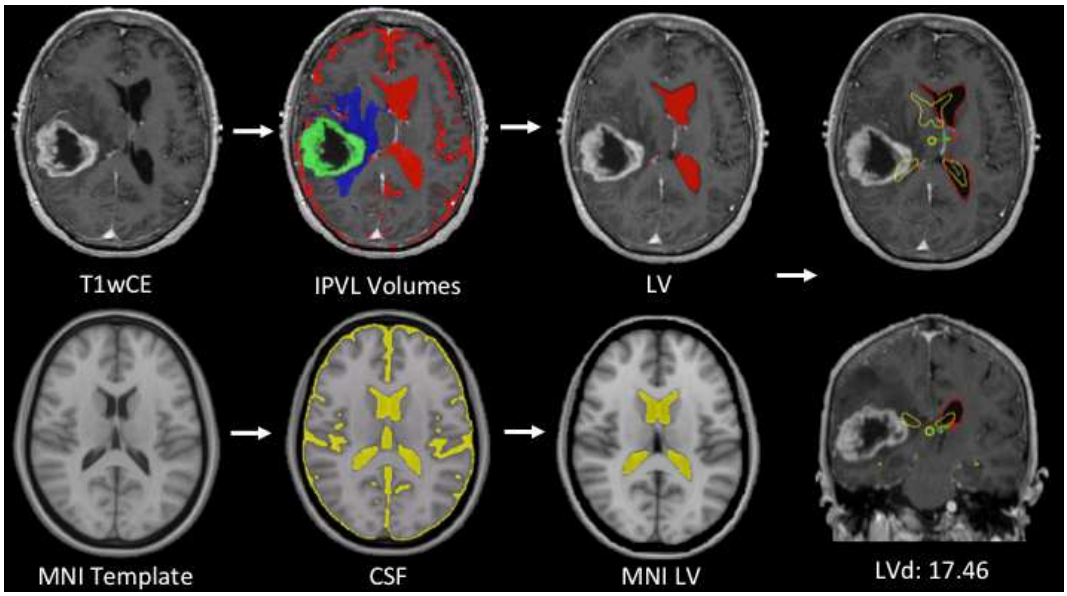

Figure 4.1. Illustrative flow of Lateral Ventricular Displacement (LVd) calculation. Top: Images are automatically segmented into the constituent tissue compartments to extract the CSF volume in patients with tumor. Bottom: The same segmentation is performed on the MNI template to derive a theoretical "normal" CSF volume. The vector representing the displacement of the center of mass of the "normal" CSF to the tumor CSF is calculated. The resultant magnitude is the magnitude of LVd.

4.3. Results

4.3.1. LVd shifts occur in a majority of glioblastoma tumor patients

We calculated LVd for 194 subjects from the TCGA cohort. An example of these calculations and demonstration of the range of LVd in our sample can be found in Figure 4.2. To better characterize our measure we performed LVd quantification in 550 subjects from a publically available non-tumor neuro imaging cohort (Information eXtraction from Images dataset, Biomedical Image Analysis Group, Imperial College London, www.biomedic.doc.ic.ac.uk/brain-development/index). Demographics for these subjects can be found in Table 4.1. This task was performed to characterize the extent of LVD in normal subjects while ensuring that the degree of LVd seen in non-tumor subjects was significantly different than the degree of shift seen in patients with glioblastoma. We found that all control subjects had an LVd less than 6.5 mm, while the vast majority of tumor patients (77%) had an LVd above 6.5 mm. In the IXI normal imaging cohort the average LVd was 3.22 mm ranging from 0.53 to 6.46 mm. The 194 glioblastoma subjects from the TCIA had significantly higher LVd measures with an average of 10.93 mm ranging from 1.88 to 29.11 mm ($t = 30.16$, $p < .001$). Histograms of the distributions of LVD from both cohorts can be found in Figure 4.3. It is important to point out that nearly 30% of patients with presurgical glioblastoma have LVds within normal ranges in our cohort. Patients with these “normal”

levels of LVd had more than 100 days longer median survival time relative to glioblastoma patients

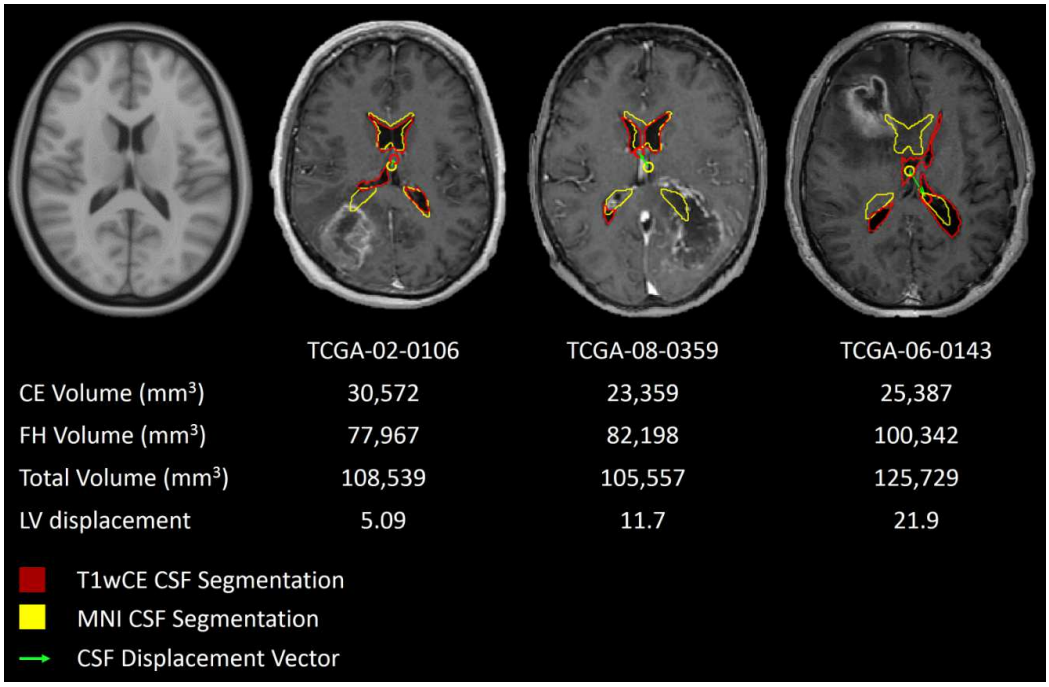

Figure 4.2. Patients with similar tumor volumes can have differing levels of LVd. Examples from a MNI axial slice z=87 representing the range of CSF displacement magnitudes from the TCGA cohort. Red indicates the borders of the T1wCE CSF lateral ventricular segmentation, while yellow indicates the segmentation of the MNI lateral ventricles. The component vector of displacement is plotted in green for each figure. The sample names, contrast enhancement (CE) volume, and lateral ventricle (LV) displacement is printed below each figure.

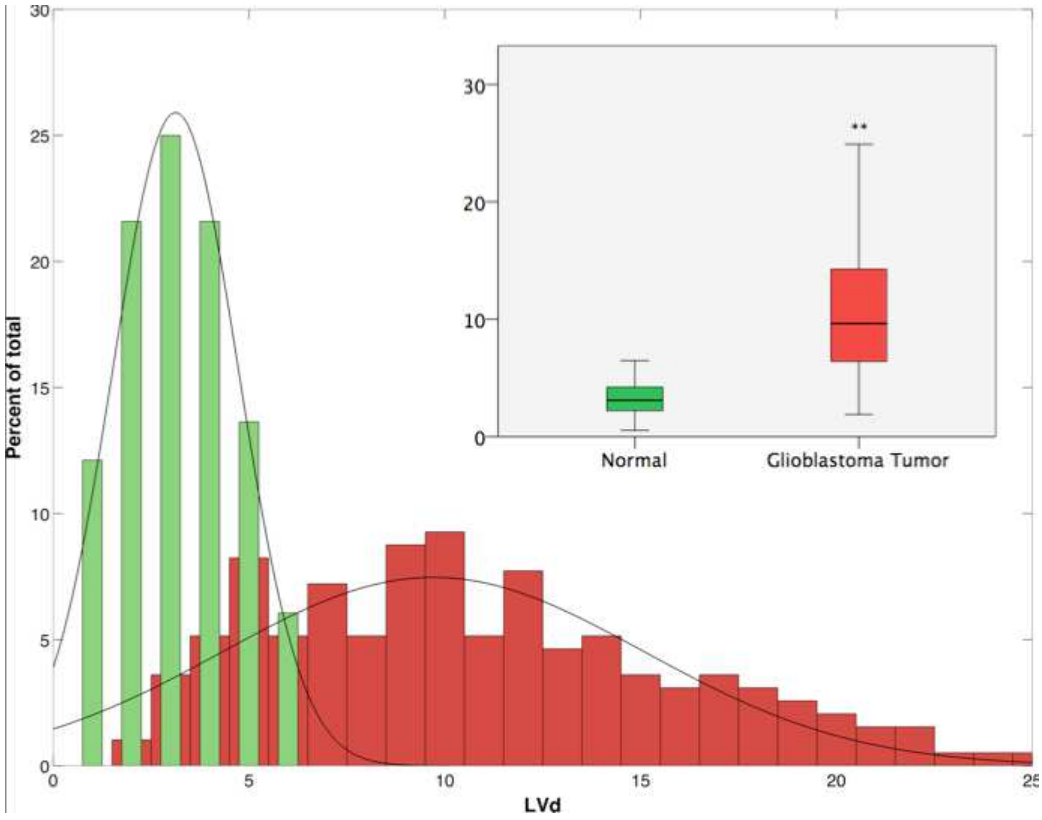

Figure 4.3. LVds occur in a majority of glioblastoma tumor patients. Right: Boxplot illustrating the difference in mean and variance of LVd in both normal and tumor cohorts. glioblastoma tumors showed a significantly higher mean LVd. ** $p < .0001$. Left: Histogram demonstrating the distribution of LVd magnitude in a normal cohort (green) and glioblastoma tumor subjects (red).

4.3.2. The variance of LVd is not solely explained by tumor volume

We observed that subjects displayed differential LVd with respect to tumor size across our cohort. In order to investigate the role of tumor size on LVd, we plotted LVd with respect to contrast enhancing volume (CEV), FLAIR hyperintensity volume (FHV), and total tumor volume (CEV+FHV) (Figure 4.4). Linear regression between CEV, FHV, and LVd revealed a Pearson correlation R^2 value of only 0.55. These results suggest that CEV and FHV alone do not explain entirely the variance of the LVd measurement.

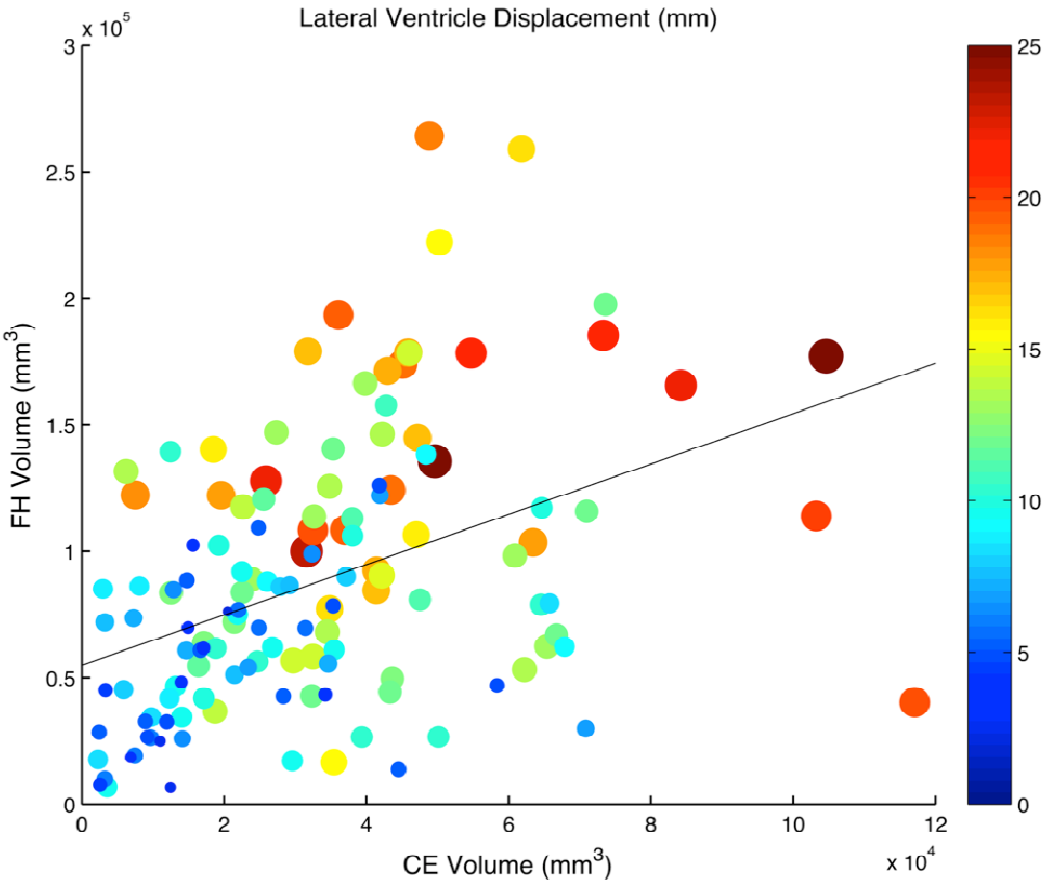

Figure 4.4. Subjects with similar tumor volumes can have differing levels of LVd. Examples a MNI axial slice z87 representing the range of CSF displacement magnitudes from the TCGA cohort. Red indicates the borders of the T1wCE CSF lateral ventricular segmentation, while yellow indicates the segmentation of the MNI lateral ventricles. The component vector of displacement is plotted in green for each figure. The sample names, contrast enhancement (CE) volume, and lateral ventricle (LV) displacement is printed below each figure.

4.3.3. Glioblastoma patients with higher LVd demonstrate poorer survival

We hypothesized that LVd, our proxy measurement for tumor mass effect, would associate with patient survival. To investigate this relationship, we first performed univariate Cox regression with respect to LVd in our TCIA cohort of 194 subjects. This analysis confirmed that LVd is associated with reduced patient survival ($p = 0.007$). When each patient's age at diagnosis, a known survival associated measure, was added to the Cox regression model, LVd remained significantly associated with reduced patient survival ($p = 0.006$, Figure 4.5). This was also true while including patients' KPS scores. When LVd was dichotomized by its median, Kaplan-Meier survival analysis revealed that high LVd was, again, strongly associated with reduced patient survival. (Log-rank $p = 0.02$, Figure 4.5). CEV was associated with survival by univariate Cox regression ($p = 0.05$), while FHV was not associated with survival in our cohort. When combined with LVd in a Cox model, the CEV term lost significance. In a prior study, we observed that patients with tumors adjacent to the subventricular zone (SVZ) have poorer survival than patients with higher SVZ distances (Chapter 3, manuscript in preparation). In order to confirm that the effect of mass effect on survival was independent of SVZ distance, we combined SVZ distance, LVD, and age into a Cox model, and all features remained significantly associated with survival (Table 4.1). Furthermore, when combined by median cutoff, patients with lower SVZ distance and higher LVD showed the worst survival of all groups in Kaplan-Meier analysis (Figure 4.5)

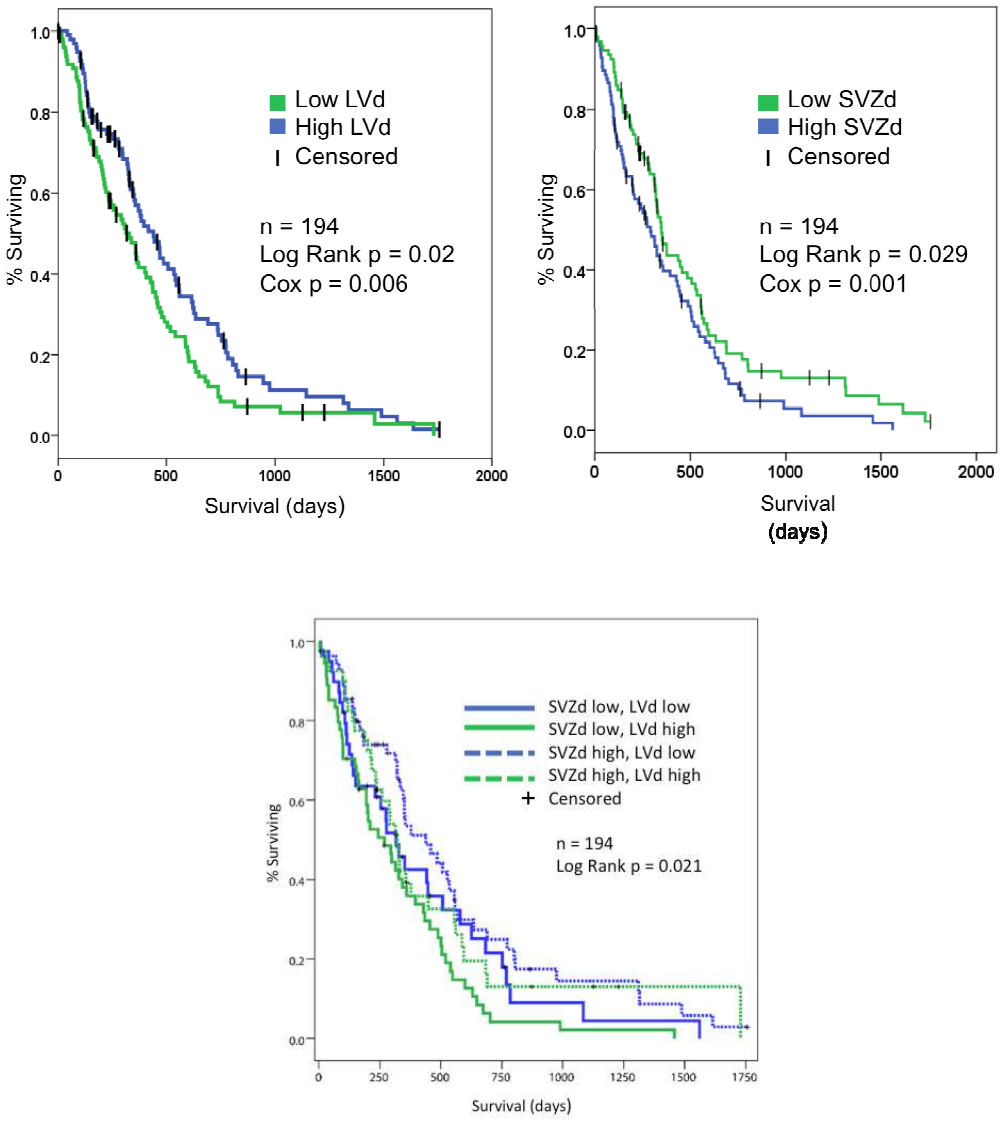

Figure 4.5. Increased LVd is a strongly associated with poorer patient survival and increased SVZ distance is a strongly associated with longer patient survival. Left: Kaplan-Meier survival curve derived from a median cutoff of LVd distribution in the TCGA cohort. Higher levels of LVd are associated with decreased survival (p=0.02 log rank, n=194). Table 4.1 contains the Cox regression analysis showing that LVd remains significantly associated with survival despite covarying for age (p=0.006). Right: Kaplan-Meier survival curve derived from a median cutoff of SVZ distance distribution in the TCGA cohort. Higher levels of SVZ distance are associated with prolonged survival (p=0.029 log rank, n=194). Table 4.1 contains the Cox regression analysis showing that LVd remains significantly associated with survival despite covarying for age (p=0.001). Bottom: Combined Kaplan-Meier curves for 4 groups based on median cut-offs of SVZd and LVD.

Table 4.1. Cox Regression analysis with LVd, SVZd, and age

Model (-2 Log Likelihood)	*B*	e^B	*SE*	*p*
LVd*Age (1315.23)				
LVd	0.043	1.044	0.016	0.006
Age	0.031	1.032	0.001	0.001
SVZd*Age (1321.78)				
SVZd	-0.036	0.965	0.009	0.001
Age	0.032	1.033	0.008	0.001
LVd*SVZd*Age (1306.56)				
LVd	0.038	1.038	0.015	0.008
SVZd	0.033	1.034	0.007	0.001
Age	-0.034	0.967	0.01	0.003

4.3.4. Differential expression analysis identifies that biosynthetic pathways, and genes tied to oxidative phosphorylation are upregulated, while neural differentiation factors are downregulated in tumors with high LVd.

Differential expression analyses were performed in both the Agilent HT-HG-U133a mRNA level III and mRNAseq expression sets. Each gene was independently correlated with LVd by Spearman correlation and nominal p values were corrected for multiple comparisons using Benjamini Hochberg correction[79]. Genes which showed greater than two-fold change and significant association with LVd were kept and consolidated into an LVd associated signature. Using previously published methods, single sample gene set enrichment analysis (ssGSEA)[54] was used to calculate enrichment scores for signatures pulled from MsigDB for each subject in the TCGA cohort. These signatures were tested for correlation with the LVD measure, along with the LVD identified signature (Figure 4.6).

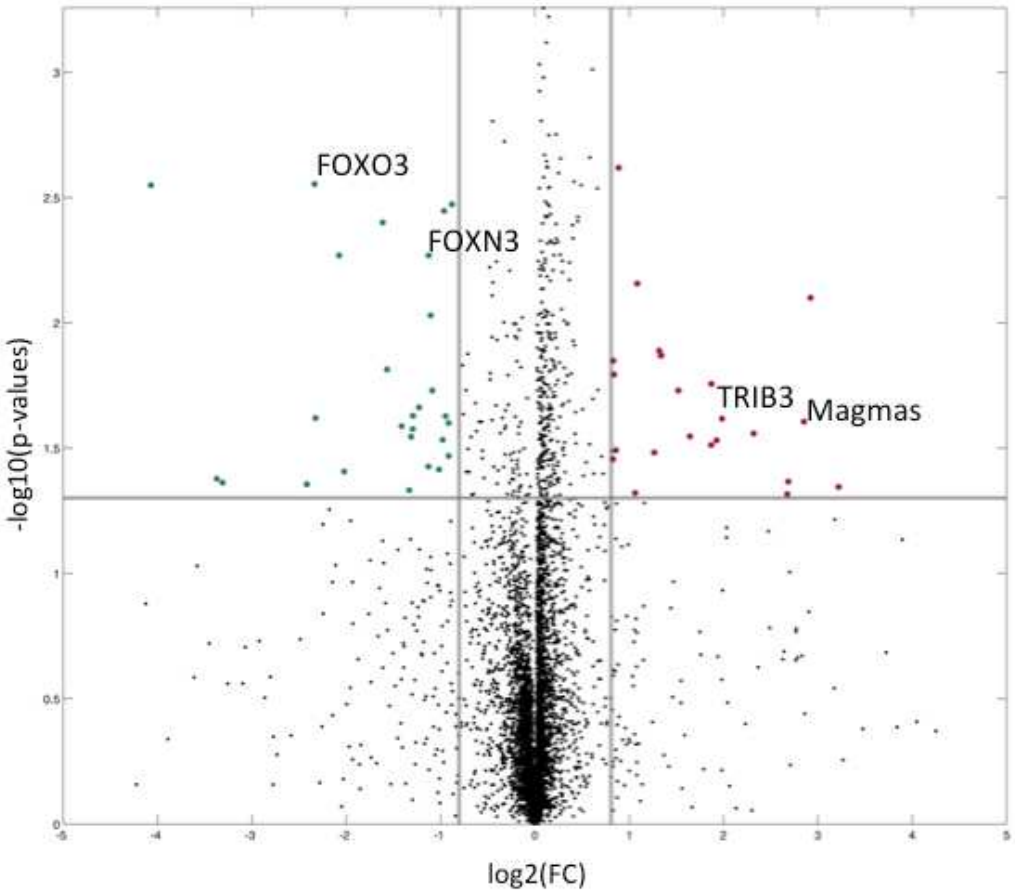

Figure 4.6. Differential expression analysis reveals genes associated with LVd: Volcano plot illustrating the genes upregulated in high LVd (at right in red), and genes downregulated in high LVd (at left in green). Log 2 of fold change is denoted on the x- axis.

4.4. Discussion

In this study, we define and characterize a novel quantitative radiographic parameter termed LVd. This noninvasive measure, a proxy for mass effect, associates with poor overall survival and could be used to evaluate patients with glioblastoma. LVd is novel quantitative measure of mass effect which associates with survival in the TCIA glioblastoma cohort, demonstrating its potential in aiding prognosis. Use of LVd in this cohort has identified genes which may be associated with the mass effect phenotype. Application of quantitative radiographic parameters, like LVd, to the study of glioblastoma opens up new possibilities for elucidating the complex mechanisms which govern this disease.

Glioblastoma is the most common and deadliest form of brain cancer[6].Chief among the challenges to glioblastoma treatment, is its heterogeneous multiform nature, which demands researchers pursue integrated approaches to unravel its complex physiology[8]. Considering that the clinical management of glioblastoma relies heavily on magnetic resonance imaging, it seems logical quantitative applications of MR parameters may help clinicians identify prognostic clues and begin to uncover the complexity of glioblastoma through the lens of observable and measurable phenotypes. One such radiographic parameter is presented here: LVd, a proxy for mass effect, is a feature which we show possesses prognostic utility.

To characterize the extent of LVd variation we see in non-tumor subjects we analyzed 550 age-matched subjects from the IXI control neuroimaging cohort. We found that despite the range of anatomical variations, normal subjects have significantly lower LVd relative to patients with glioblastoma tumors. These data suggest that LVd can accurately identify the effect of tumor on the intracranial compartments.

The degree of displacement of the lateral ventricles may be a factor of more than just tumor volume. A linear regression revealed that LVd was weakly positively correlated with CE and FH volume. This suggests that while tumor volume may explain a portion of LVd, tumor volume cannot explain the entirety of LVd variance. Other factors that may contribute include erosion and transformation of surrounding parenchyma. We identified many tumors with low volume and high LVd as well as others with high volume and low LVd. In addition, 30% of patients with glioblastoma had LVds within the range found in our control cohort. We show that LVd is not solely explained by tumor volume. Furthermore, Cox analysis demonstrated that while LVd has a strong association with decreased survival, CE and FH volume did not have a significant association. Therefore, LVd may provide additional insight into tumor pathophysiology than tumor volume alone.

We found that LVD was associated with reduced patient survival ($p=0.007$). This association was independent of age, KPS score, and tumor volume. We have previously shown that proximity to the subventricular zone (SVZ) was associated with decreased patient survival. Tumors near the SVZ

are closer to the ventricles, may also have elevated LVd, and therefore may explain the survival association with LVd. However, we found that again, LVd's association with decreased survival was an independent effect. Together, proximity to the SVZ and increased LVd both contribute to poor patient survival.

The objective of our genomic analysis was to identify genes related to LVd and therefore mass effect. Before employing differential expression analysis we hypothesized generally that we would identify pro-growth genes in patients with high LVd, and growth arrestors in patients with lower LVd. Growth restricting neural differentiation cues were identified among the signature as down regulated in patients with high LVD. These genes included FOXO3, FOXN3, and BMPR2 which have been implicated as controllers of stem cell differentiation and reducers of glioblastoma tumorogenicity[80-82]. Other tumor suppressor candidates were also identified like NEO 1 neoginin[83, 84]. To validate these results we downloaded a signature of genes that are significantly down-regulated by oncogenic mir-21, in a glioblastoma cell line A172[85]. This gene set was available from the Broad Institute's curated Molecular Signatures Database and was used to perform ssGSEA to calculate enrichment scores for all subjects in our cohort. We found that LVd was significantly and negatively correlated with tumor suppressors that are transcriptionally repressed by mir-21.

Surprisingly, genes related to oxidative phosphorylation, and aerobic respiration were up-regulated in subjects with high LVd. This result was

confirmed using DAVID functional annotation (http://david.abcc.ncifcrf.gov/), which showed a strong enrichment for genes related to processes of aerobic respiration. To confirm whether the entire aerobic respiration pathway was enriched as a function of LVd, we pulled an aerobic respiration gene signature from the Molecular Signatures Database from the Broad Instistute and performed ssGSEA to calculate enrichment scores for all subjects within our cohort. We found that this entire signature correlated with LVd ($r = 0.15$, $p = 0.04$). It is possible given this result that tumors with increased aerobic respiration would have more efficient metabolic machinery, allowing them to expand at a much faster rate than tumors relying on glycolysis. Tumors of this rapidly dividing subtype may allow less time for the brain to accommodate their growing mass and exhibit greater LVd than a slower growing tumor of equal volume.

Though we are thankful for the wealth of data afforded to us by the TCIA, our study is inherently limited by the wide variation of imaging availability and myriad different scans, resolutions, and protocols, that were employed. We addressed this limitation by employing IPVL automated segmentation to the data set that was designed to handle heterogenous datasets, and carefully reviewed all steps of or processing through image segmentation to ensure both accuracy and quality of our results. Although our study represents 194 subjects from multiple different sites around the country, we would like to see further validation in other cohorts to confirm its findings. Ultimately, we hope the integration of parameters like LVd along with clinical

and genomic profiling data will furnish researchers and clinicians with the tools necessary to design new therapeutics, monitor treatment response and tumor progression, and ultimately improve the lives of patients afflicted by glioblastoma.

Chapter 4, in part, is now in preparation for submission for publication of the material. Tyler C. Steed, Jeffrey M. Treiber, Kunal Patel, Bob S. Carter, Anders M. Dale, and Clark C. Chen (2014). Tentatively entitled “Quantification of lateral ventricle displacement magnitude in glioblastoma imaging associates with decreased patient survival. The dissertation/thesis author was the primary investigator and author of this material.

5. Conclusions and Future Studies

The results of this thesis establish the utility of radiogenomics to supplement clinical and molecular profiling data. Taken together, these results support the idea that radiographic features derived from glioblastoma imaging correlate with gene expression and molecular alterations. Additionally, we demonstrate that tumor imaging may prove to be a convenient, ubiquitous, and noninvasive tool helping to evaluate tumor biology.

Although the entirety of the results presented here were derived from retrospective study, validation for research pertaining to radiogenomics will require prospective evaluation. It is important to remember that the biological state of glioblastoma is not static. It is well-known that profound molecular changes occur in response to immune interaction and therapeutic strategy. Bearing this in mind, future studies may derive benefit from following longitudinal changes in imaging serially. Application of the strategy may prove of particular importance in the evaluation of clinical trials. Additionally, while the radiographic parameters described in this thesis independently associated with survival, there are a number of more simple radiographic features which may not. Although these features may not associate with survival, they may nevertheless associate with patterns of differential genomic expression representing unique biological states. Classification, identification, and

combination of biologically important radiographic parameters into new radiophenotypes may provide added context for molecular profiling data.

As we move forward into the era of personalized medicine, thoughtful extraction and careful integration of pertinent information will be required to make optimal decisions leading to better patient outcomes. Ultimately, imaging parameters like those described herein, will provide the necessary metrics to help researchers and clinicians discover new therapeutics, monitor evaluate treatment response, and change the lives of patients afflicted with glioblastoma.

REFERENCES

1. Ostrom, Q.T., H. Gittleman, P. Farah, A. Ondracek, Y. Chen, Y. Wolinsky, N.E. Stroup, C. Kruchko, and J.S. Barnholtz-Sloan, *CBTRUS statistical report: Primary brain and central nervous system tumors diagnosed in the United States in 2006-2010.* Neuro Oncol, 2013. **15 Suppl 2**: p. ii1-56.

2. Johnson, D.R. and B.P. O'Neill, *Glioblastoma survival in the United States before and during the temozolomide era.* J Neurooncol, 2012. **107**(2): p. 359-64.

3. Belden, C.J., P.A. Valdes, C. Ran, D.A. Pastel, B.T. Harris, C.E. Fadul, M.A. Israel, K. Paulsen, and D.W. Roberts, *Genetics of glioblastoma: a window into its imaging and histopathologic variability.* Radiographics, 2011. **31**(6): p. 1717-40.

4. Cancer Genome Atlas Research, N., *Comprehensive genomic characterization defines human glioblastoma genes and core pathways.* Nature, 2008. **455**(7216): p. 1061-8.

5. Noushmehr, H., D.J. Weisenberger, K. Diefes, H.S. Phillips, K. Pujara, B.P. Berman, F. Pan, C.E. Pelloski, E.P. Sulman, K.P. Bhat, R.G. Verhaak, K.A. Hoadley, D.N. Hayes, C.M. Perou, H.K. Schmidt, L. Ding, R.K. Wilson, D. Van Den Berg, H. Shen, H. Bengtsson, P. Neuvial, L.M. Cope, J. Buckley, J.G. Herman, S.B. Baylin, P.W. Laird, K. Aldape, and N. Cancer Genome Atlas Research, *Identification of a CpG island methylator phenotype that defines a distinct subgroup of glioma.* Cancer Cell, 2010. **17**(5): p. 510-22.

6. Omuro, A. and L.M. DeAngelis, *Glioblastoma and other malignant gliomas: a clinical review.* JAMA, 2013. **310**(17): p. 1842-50.

7. Minniti, G., R. Muni, G. Lanzetta, P. Marchetti, and R.M. Enrici, *Chemotherapy for glioblastoma: current treatment and future perspectives for cytotoxic and targeted agents.* Anticancer Res, 2009. **29**(12): p. 5171-84.

8. Brennan, C.W., R.G. Verhaak, A. McKenna, B. Campos, H. Noushmehr, S.R. Salama, S. Zheng, D. Chakravarty, J.Z. Sanborn, S.H. Berman, R. Beroukhim, B. Bernard, C.J. Wu, G. Genovese, I. Shmulevich, J. Barnholtz-Sloan, L. Zou, R. Vegesna, S.A. Shukla, G. Ciriello, W.K. Yung, W. Zhang, C. Sougnez, T. Mikkelsen, K. Aldape, D.D. Bigner, E.G. Van Meir, M. Prados, A. Sloan, K.L. Black, J. Eschbacher, G. Finocchiaro, W. Friedman, D.W. Andrews, A. Guha, M. Iacocca, B.P. O'Neill, G. Foltz, J. Myers, D.J. Weisenberger, R. Penny,

R. Kucherlapati, C.M. Perou, D.N. Hayes, R. Gibbs, M. Marra, G.B. Mills, E. Lander, P. Spellman, R. Wilson, C. Sander, J. Weinstein, M. Meyerson, S. Gabriel, P.W. Laird, D. Haussler, G. Getz, L. Chin, and T.R. Network, *The somatic genomic landscape of glioblastoma.* Cell, 2013. **155**(2): p. 462-77.

9. Diehn, M., C. Nardini, D.S. Wang, S. McGovern, M. Jayaraman, Y. Liang, K. Aldape, S. Cha, and M.D. Kuo, *Identification of noninvasive imaging surrogates for brain tumor gene-expression modules.* Proc Natl Acad Sci U S A, 2008. **105**(13): p. 5213-8.

10. Gutman, D.A., L.A. Cooper, S.N. Hwang, C.A. Holder, J. Gao, T.D. Aurora, W.D. Dunn, L. Scarpace, T. Mikkelsen, R. Jain, M. Wintermark, M. Jilwan, P. Raghavan, E. Huang, R.J. Clifford, P. Mongkolwat, V. Kleper, J. Freymann, J. Kirby, P.O. Zinn, C.S. Moreno, C. Jaffe, R. Colen, D.L. Rubin, J. Saltz, A. Flanders, and D.J. Brat, *MR imaging predictors of molecular profile and survival: multi-institutional study of the TCGA glioblastoma data set.* Radiology, 2013. **267**(2): p. 560-9.

11. Deeley, M.A., A. Chen, R. Datteri, J.H. Noble, A.J. Cmelak, E.F. Donnelly, A.W. Malcolm, L. Moretti, J. Jaboin, K. Niermann, E.S. Yang, D.S. Yu, F. Yei, T. Koyama, G.X. Ding, and B.M. Dawant, *Comparison of manual and automatic segmentation methods for brain structures in the presence of space-occupying lesions: a multi-expert study.* Phys Med Biol, 2011. **56**(14): p. 4557-77.

12. Weltens, C., J. Menten, M. Feron, E. Bellon, P. Demaerel, F. Maes, W. Van den Bogaert, and E. van der Schueren, *Interobserver variations in gross tumor volume delineation of brain tumors on computed tomography and impact of magnetic resonance imaging.* Radiother Oncol, 2001. **60**(1): p. 49-59.

13. Zhu, Y., G.S. Young, Z. Xue, R.Y. Huang, H. You, K. Setayesh, H. Hatabu, F. Cao, and S.T. Wong, *Semi-automatic segmentation software for quantitative clinical brain glioblastoma evaluation.* Acad Radiol, 2012. **19**(8): p. 977-85.

14. Diaz, I., P. Boulanger, R. Greiner, B. Hoehn, L. Rowe, and A. Murtha, *An automatic brain tumor segmentation tool.* Conf Proc IEEE Eng Med Biol Soc, 2013. **2013**: p. 3339-42.

15. Harati, V., R. Khayati, and A. Farzan, *Fully automated tumor segmentation based on improved fuzzy connectedness algorithm in brain MR images.* Comput Biol Med, 2011. **41**(7): p. 483-92.

16. Prastawa, M., E. Bullitt, N. Moon, K. Van Leemput, and G. Gerig, *Automatic brain tumor segmentation by subject specific modification of atlas priors.* Acad Radiol, 2003. **10**(12): p. 1341-8.

17. Zikic, D., B. Glocker, E. Konukoglu, A. Criminisi, C. Demiralp, J. Shotton, O.M. Thomas, T. Das, R. Jena, and S.J. Price, *Decision forests for tissue-specific segmentation of high-grade gliomas in multi-channel MR.* Med Image Comput Comput Assist Interv, 2012. **15**(Pt 3): p. 369-76.

18. Phillips, W.E., 2nd, S. Phuphanich, R.P. Velthuizen, and M.L. Silbiger, *Automatic magnetic resonance tissue characterization for three-dimensional magnetic resonance imaging of the brain.* J Neuroimaging, 1995. **5**(3): p. 171-7.

19. Clark, M.C., L.O. Hall, D.B. Goldgof, R. Velthuizen, F.R. Murtagh, and M.S. Silbiger, *Automatic tumor segmentation using knowledge-based techniques.* IEEE Trans Med Imaging, 1998. **17**(2): p. 187-201.

20. Lee, C.H., S. Wang, A. Murtha, M.R. Brown, and R. Greiner, *Segmenting brain tumors using pseudo-conditional random fields.* Med Image Comput Comput Assist Interv, 2008. **11**(Pt 1): p. 359-66.

21. Prastawa, M., E. Bullitt, S. Ho, and G. Gerig, *A brain tumor segmentation framework based on outlier detection.* Med Image Anal, 2004. **8**(3): p. 275-83.

22. Menze, B., K. van Leemput, D. Lashkari, M.-A. Weber, N. Ayache, and P. Golland, *A Generative Model for Brain Tumor Segmentation in Multi-Modal Images*, in *Medical Image Computing and Computer-Assisted Intervention – MICCAI 2010*, T. Jiang, et al., Editors. 2010, Springer Berlin Heidelberg. p. 151-159.

23. Gordillo, N., E. Montseny, and P. Sobrevilla, *State of the art survey on MRI brain tumor segmentation.* Magn Reson Imaging, 2013. **31**(8): p. 1426-38.

24. Jenkinson, M., C.F. Beckmann, T.E. Behrens, M.W. Woolrich, and S.M. Smith, *Fsl.* Neuroimage, 2012. **62**(2): p. 782-90.

25. Smith, S.M., M. Jenkinson, M.W. Woolrich, C.F. Beckmann, T.E. Behrens, H. Johansen-Berg, P.R. Bannister, M. De Luca, I. Drobnjak, D.E. Flitney, R.K. Niazy, J. Saunders, J. Vickers, Y. Zhang, N. De Stefano, J.M. Brady, and P.M. Matthews, *Advances in functional and structural MR image analysis and implementation as FSL.* Neuroimage, 2004. **23 Suppl 1**: p. S208-19.

26. Dale, A.M., B. Fischl, and M.I. Sereno, *Cortical surface-based analysis. I. Segmentation and surface reconstruction.* Neuroimage, 1999. **9**(2): p. 179-94.

27. Jovicich, J., S. Czanner, D. Greve, E. Haley, A. van der Kouwe, R. Gollub, D. Kennedy, F. Schmitt, G. Brown, J. Macfall, B. Fischl, and A. Dale, *Reliability in multi-site structural MRI studies: effects of gradient non-linearity correction on phantom and human data.* Neuroimage, 2006. **30**(2): p. 436-43.

28. Holland, D., J.M. Kuperman, and A.M. Dale, *Efficient correction of inhomogeneous static magnetic field-induced distortion in Echo Planar Imaging.* Neuroimage, 2010. **50**(1): p. 175-83.

29. Smith, S.M., *Fast robust automated brain extraction.* Hum Brain Mapp, 2002. **17**(3): p. 143-55.

30. Grabner, G., A.L. Janke, M.M. Budge, D. Smith, J. Pruessner, and D.L. Collins, *Symmetric atlasing and model based segmentation: an application to the hippocampus in older adults.* Med Image Comput Comput Assist Interv, 2006. **9**(Pt 2): p. 58-66.

31. Jenkinson, M. and S. Smith, *A global optimisation method for robust affine registration of brain images.* Med Image Anal, 2001. **5**(2): p. 143-56.

32. Jenkinson, M., P. Bannister, M. Brady, and S. Smith, *Improved optimization for the robust and accurate linear registration and motion correction of brain images.* Neuroimage, 2002. **17**(2): p. 825-41.

33. Iglesias, J.E., C.Y. Liu, P.M. Thompson, and Z. Tu, *Robust brain extraction across datasets and comparison with publicly available methods.* IEEE Trans Med Imaging, 2011. **30**(9): p. 1617-34.

34. Otsu, N., *A Threshold Selection Method from Gray-Level Histograms.* IEEE Transactions on Systems, Man, and Cybernetics, 1979. **9**(1): p. 62-66.

35. Steenwijk, M.D., P.J. Pouwels, M. Daams, J.W. van Dalen, M.W. Caan, E. Richard, F. Barkhof, and H. Vrenken, *Accurate white matter lesion segmentation by k nearest neighbor classification with tissue type priors (kNN-TTPs).* Neuroimage Clin, 2013. **3**: p. 462-9.

36. Anbeek, P., K.L. Vincken, G.S. van Bochove, M.J. van Osch, and J. van der Grond, *Probabilistic segmentation of brain tissue in MR imaging.* Neuroimage, 2005. **27**(4): p. 795-804.

37. Dice, L.R., *Measures of the Amount of Ecologic Association Between Species.* Ecology, 1945. **26**(3): p. 297-302.

38. Phillips, H.S., S. Kharbanda, R. Chen, W.F. Forrest, R.H. Soriano, T.D. Wu, A. Misra, J.M. Nigro, H. Colman, L. Soroceanu, P.M. Williams, Z. Modrusan, B.G. Feuerstein, and K. Aldape, *Molecular subclasses of high-grade glioma predict prognosis, delineate a pattern of disease progression, and resemble stages in neurogenesis.* Cancer Cell, 2006. **9**(3): p. 157-73.

39. Verhaak, R.G., K.A. Hoadley, E. Purdom, V. Wang, Y. Qi, M.D. Wilkerson, C.R. Miller, L. Ding, T. Golub, J.P. Mesirov, G. Alexe, M. Lawrence, M. O'Kelly, P. Tamayo, B.A. Weir, S. Gabriel, W. Winckler, S. Gupta, L. Jakkula, H.S. Feiler, J.G. Hodgson, C.D. James, J.N. Sarkaria, C. Brennan, A. Kahn, P.T. Spellman, R.K. Wilson, T.P. Speed, J.W. Gray, M. Meyerson, G. Getz, C.M. Perou, D.N. Hayes, and N. Cancer Genome Atlas Research, *Integrated genomic analysis identifies clinically relevant subtypes of glioblastoma characterized by abnormalities in PDGFRA, IDH1, EGFR, and NF1.* Cancer Cell, 2010. **17**(1): p. 98-110.

40. Sanai, N., T. Nguyen, R.A. Ihrie, Z. Mirzadeh, H.H. Tsai, M. Wong, N. Gupta, M.S. Berger, E. Huang, J.M. Garcia-Verdugo, D.H. Rowitch, and A. Alvarez-Buylla, *Corridors of migrating neurons in the human brain and their decline during infancy.* Nature, 2011. **478**(7369): p. 382-6.

41. Eriksson, P.S., E. Perfilieva, T. Bjork-Eriksson, A.M. Alborn, C. Nordborg, D.A. Peterson, and F.H. Gage, *Neurogenesis in the adult human hippocampus.* Nat Med, 1998. **4**(11): p. 1313-7.

42. Quinones-Hinojosa, A., N. Sanai, O. Gonzalez-Perez, and J.M. Garcia-Verdugo, *The human brain subventricular zone: stem cells in this niche and its organization.* Neurosurg Clin N Am, 2007. **18**(1): p. 15-20, vii.

43. Sakaguchi, M. and H. Okano, *Neural stem cells, adult neurogenesis, and galectin-1: from bench to bedside.* Dev Neurobiol, 2012. **72**(7): p. 1059-67.

44. Taupin, P. and F.H. Gage, *Adult neurogenesis and neural stem cells of the central nervous system in mammals.* J Neurosci Res, 2002. **69**(6): p. 745-9.

45. Rakic, P., *Principles of neural cell migration.* Experientia, 1990. **46**(9): p. 882-91.

46. Sanai, N., A. Alvarez-Buylla, and M.S. Berger, *Neural stem cells and the origin of gliomas.* N Engl J Med, 2005. **353**(8): p. 811-22.

47. Lim, D.A., S. Cha, M.C. Mayo, M.H. Chen, E. Keles, S. VandenBerg, and M.S. Berger, *Relationship of glioblastoma multiforme to neural stem cell regions predicts invasive and multifocal tumor phenotype.* Neuro Oncol, 2007. **9**(4): p. 424-9.

48. Marino, S., M. Vooijs, H. van Der Gulden, J. Jonkers, and A. Berns, *Induction of medulloblastomas in p53-null mutant mice by somatic inactivation of Rb in the external granular layer cells of the cerebellum.* Genes Dev, 2000. **14**(8): p. 994-1004.

49. Lai, A., S. Kharbanda, W.B. Pope, A. Tran, O.E. Solis, F. Peale, W.F. Forrest, K. Pujara, J.A. Carrillo, A. Pandita, B.M. Ellingson, C.W. Bowers, R.H. Soriano, N.O. Schmidt, S. Mohan, W.H. Yong, S. Seshagiri, Z. Modrusan, Z. Jiang, K.D. Aldape, P.S. Mischel, L.M. Liau, C.J. Escovedo, W. Chen, P.L. Nghiemphu, C.D. James, M.D. Prados, M. Westphal, K. Lamszus, T. Cloughesy, and H.S. Phillips, *Evidence for sequenced molecular evolution of IDH1 mutant glioblastoma from a distinct cell of origin.* J Clin Oncol, 2011. **29**(34): p. 4482-90.

50. Zlatescu, M.C., A. TehraniYazdi, H. Sasaki, J.F. Megyesi, R.A. Betensky, D.N. Louis, and J.G. Cairncross, *Tumor location and growth pattern correlate with genetic signature in oligodendroglial neoplasms.* Cancer Res, 2001. **61**(18): p. 6713-5.

51. Steed, T.C., J.M. Treiber, K.S. Patel, Z. Taich, N.S. White, M.L. Treiber, N. Farid, B.S. Carter, A.M. Dale, and C.C. Chen, *Iterative Probabilistic Voxel Labeling: Automated Segmentation for Analysis of The Cancer Imaging Archive Glioblastoma Images.* AJNR Am J Neuroradiol, 2014.

52. Irizarry, R.A., B. Hobbs, F. Collin, Y.D. Beazer-Barclay, K.J. Antonellis, U. Scherf, and T.P. Speed, *Exploration, normalization, and summaries of high density oligonucleotide array probe level data.* Biostatistics, 2003. **4**(2): p. 249-64.

53. Li, B. and C.N. Dewey, *RSEM: accurate transcript quantification from RNA-Seq data with or without a reference genome.* BMC Bioinformatics, 2011. **12**: p. 323.

54. Barbie, D.A., P. Tamayo, J.S. Boehm, S.Y. Kim, S.E. Moody, I.F. Dunn, A.C. Schinzel, P. Sandy, E. Meylan, C. Scholl, S. Frohling, E.M. Chan, M.L. Sos, K. Michel, C. Mermel, S.J. Silver, B.A. Weir, J.H. Reiling, Q. Sheng, P.B. Gupta, R.C. Wadlow, H. Le, S. Hoersch, B.S. Wittner, S. Ramaswamy, D.M. Livingston, D.M. Sabatini, M. Meyerson, R.K.

Thomas, E.S. Lander, J.P. Mesirov, D.E. Root, D.G. Gilliland, T. Jacks, and W.C. Hahn, *Systematic RNA interference reveals that oncogenic KRAS-driven cancers require TBK1.* Nature, 2009. **462**(7269): p. 108-12.

55. Gooya, A., K.M. Pohl, M. Bilello, L. Cirillo, G. Biros, E.R. Melhem, and C. Davatzikos, *GLISTR: glioma image segmentation and registration.* IEEE Trans Med Imaging, 2012. **31**(10): p. 1941-54.

56. Tustison, N.J., B.B. Avants, P.A. Cook, Y. Zheng, A. Egan, P.A. Yushkevich, and J.C. Gee, *N4ITK: improved N3 bias correction.* IEEE Trans Med Imaging, 2010. **29**(6): p. 1310-20.

57. Avants, B.B., N.J. Tustison, M. Stauffer, G. Song, B. Wu, and J.C. Gee, *The Insight ToolKit image registration framework.* Front Neuroinform, 2014. **8**: p. 44.

58. Ellingson, B.M., T.F. Cloughesy, W.B. Pope, T.M. Zaw, H. Phillips, S. Lalezari, P.L. Nghiemphu, H. Ibrahim, K.M. Naeini, R.J. Harris, and A. Lai, *Anatomic localization of O6-methylguanine DNA methyltransferase (MGMT) promoter methylated and unmethylated tumors: a radiographic study in 358 de novo human glioblastomas.* Neuroimage, 2012. **59**(2): p. 908-16.

59. The Mathworks, I., *MATLAB and Statistics Toolbox Release 2012b*. Natick, MA, United States.

60. Ellingson, B.M., A. Lai, R.J. Harris, J.M. Selfridge, W.H. Yong, K. Das, W.B. Pope, P.L. Nghiemphu, H.V. Vinters, L.M. Liau, P.S. Mischel, and T.F. Cloughesy, *Probabilistic radiographic atlas of glioblastoma phenotypes.* AJNR Am J Neuroradiol, 2013. **34**(3): p. 533-40.

61. Reynolds, B.A. and S. Weiss, *Generation of neurons and astrocytes from isolated cells of the adult mammalian central nervous system.* Science, 1992. **255**(5052): p. 1707-10.

62. Singh, S.K., I.D. Clarke, M. Terasaki, V.E. Bonn, C. Hawkins, J. Squire, and P.B. Dirks, *Identification of a cancer stem cell in human brain tumors.* Cancer Res, 2003. **63**(18): p. 5821-8.

63. Pojo, M., C.S. Goncalves, A. Xavier-Magalhaes, A.I. Oliveira, T. Goncalves, S. Correia, A.J. Rodrigues, S. Costa, L. Pinto, A.A. Pinto, J.M. Lopes, R.M. Reis, M. Rocha, N. Sousa, and B.M. Costa, *A transcriptomic signature mediated by HOXA9 promotes human glioblastoma initiation, aggressiveness and resistance to temozolomide.* Oncotarget, 2015.

64. Murat, A., E. Migliavacca, T. Gorlia, W.L. Lambiv, T. Shay, M.F. Hamou, N. de Tribolet, L. Regli, W. Wick, M.C. Kouwenhoven, J.A. Hainfellner, F.L. Heppner, P.Y. Dietrich, Y. Zimmer, J.G. Cairncross, R.C. Janzer, E. Domany, M. Delorenzi, R. Stupp, and M.E. Hegi, *Stem cell-related "self-renewal" signature and high epidermal growth factor receptor expression associated with resistance to concomitant chemoradiotherapy in glioblastoma.* J Clin Oncol, 2008. **26**(18): p. 3015-24.

65. Hochstim, C., B. Deneen, A. Lukaszewicz, Q. Zhou, and D.J. Anderson, *Identification of positionally distinct astrocyte subtypes whose identities are specified by a homeodomain code.* Cell, 2008. **133**(3): p. 510-22.

66. Hugdahl, K., *Signs of cognitive decline in the elderly population.* J Nutr Health Aging, 2010. **14**(9): p. 750.

67. Toga, A.W. and P.M. Thompson, *Mapping brain asymmetry.* Nat Rev Neurosci, 2003. **4**(1): p. 37-48.

68. Sun, T., C. Patoine, A. Abu-Khalil, J. Visvader, E. Sum, T.J. Cherry, S.H. Orkin, D.H. Geschwind, and C.A. Walsh, *Early asymmetry of gene transcription in embryonic human left and right cerebral cortex.* Science, 2005. **308**(5729): p. 1794-8.

69. Sun, T. and C.A. Walsh, *Molecular approaches to brain asymmetry and handedness.* Nat Rev Neurosci, 2006. **7**(8): p. 655-62.

70. Li, J., S. Zhu, D. Kozono, K. Ng, D. Futalan, Y. Shen, J.C. Akers, T. Steed, D. Kushwaha, M. Schlabach, B.S. Carter, C.H. Kwon, F. Furnari, W. Cavenee, S. Elledge, and C.C. Chen, *Genome-wide shRNA screen revealed integrated mitogenic signaling between dopamine receptor D2 (DRD2) and epidermal growth factor receptor (EGFR) in glioblastoma.* Oncotarget, 2014. **5**(4): p. 882-93.

71. Simpson, J.R., J. Horton, C. Scott, W.J. Curran, P. Rubin, J. Fischbach, S. Isaacson, M. Rotman, S.O. Asbell, and J.S. Nelson, *Influence of location and extent of surgical resection on survival of patients with glioblastoma multiforme: results of three consecutive Radiation Therapy Oncology Group (RTOG) clinical trials.* Int J Radiat Oncol Biol Phys, 1993. **26**(2): p. 239-44.

72. Mokri, B., *The Monro-Kellie hypothesis: applications in CSF volume depletion.* Neurology, 2001. **56**(12): p. 1746-8.

73. Zazulia, A.R., M.N. Diringer, C.P. Derdeyn, and W.J. Powers, *Progression of mass effect after intracerebral hemorrhage.* Stroke, 1999. **30**(6): p. 1167-73.

74. Tu, P.H., Z.H. Liu, C.C. Chuang, T.C. Yang, C.T. Wu, and S.T. Lee, *Postoperative midline shift as secondary screening for the long-term outcomes of surgical decompression of malignant middle cerebral artery infarcts.* J Clin Neurosci, 2012. **19**(5): p. 661-4.

75. Kim, J.J. and A.D. Gean, *Imaging for the diagnosis and management of traumatic brain injury.* Neurotherapeutics, 2011. **8**(1): p. 39-53.

76. Li, G.Z., J. Yang, C.Z. Ye, and D.Y. Geng, *Degree prediction of malignancy in brain glioma using support vector machines.* Comput Biol Med, 2006. **36**(3): p. 313-25.

77. Lacroix, M., D. Abi-Said, D.R. Fourney, Z.L. Gokaslan, W. Shi, F. DeMonte, F.F. Lang, I.E. McCutcheon, S.J. Hassenbusch, E. Holland, K. Hess, C. Michael, D. Miller, and R. Sawaya, *A multivariate analysis of 416 patients with glioblastoma multiforme: prognosis, extent of resection, and survival.* J Neurosurg, 2001. **95**(2): p. 190-8.

78. Zacharaki, E.I., C.S. Hogea, D. Shen, G. Biros, and C. Davatzikos, *Non-diffeomorphic registration of brain tumor images by simulating tissue loss and tumor growth.* Neuroimage, 2009. **46**(3): p. 762-74.

79. Benjamini, Y. and Y. Hochberg, *Controlling the False Discovery Rate: A Practical and Powerful Approach to Multiple Testing.* Journal of the Royal Statistical Society. Series B (Methodological), 1995. **57**(1): p. 289-300.

80. Sunayama, J., A. Sato, K. Matsuda, K. Tachibana, E. Watanabe, S. Seino, K. Suzuki, Y. Narita, S. Shibui, K. Sakurada, T. Kayama, A. Tomiyama, and C. Kitanaka, *FoxO3a functions as a key integrator of cellular signals that control glioblastoma stem-like cell differentiation and tumorigenicity.* Stem Cells, 2011. **29**(9): p. 1327-37.

81. Sato, A., J. Sunayama, M. Okada, E. Watanabe, S. Seino, K. Shibuya, K. Suzuki, Y. Narita, S. Shibui, T. Kayama, and C. Kitanaka, *Glioma-initiating cell elimination by metformin activation of FOXO3 via AMPK.* Stem Cells Transl Med, 2012. **1**(11): p. 811-24.

82. Piccirillo, S.G., B.A. Reynolds, N. Zanetti, G. Lamorte, E. Binda, G. Broggi, H. Brem, A. Olivi, F. Dimeco, and A.L. Vescovi, *Bone morphogenetic proteins inhibit the tumorigenic potential of human brain tumour-initiating cells.* Nature, 2006. **444**(7120): p. 761-5.

83. Wu, X., Y. Li, X. Wan, T.M. Kayira, R. Cao, X. Ju, X. Zhu, and G. Zhao, *Down-regulation of neogenin accelerated glioma progression through promoter Methylation and its overexpression in SHG-44 Induced Apoptosis.* PLoS One, 2012. **7**(5): p. e38074.

84. Zhou, X., Y. Ren, L. Moore, M. Mei, Y. You, P. Xu, B. Wang, G. Wang, Z. Jia, P. Pu, W. Zhang, and C. Kang, *Downregulation of miR-21 inhibits EGFR pathway and suppresses the growth of human glioblastoma cells independent of PTEN status.* Lab Invest, 2010. **90**(2): p. 144-55.

85. Gabriely, G., T. Wurdinger, S. Kesari, C.C. Esau, J. Burchard, P.S. Linsley, and A.M. Krichevsky, *MicroRNA 21 promotes glioma invasion by targeting matrix metalloproteinase regulators.* Mol Cell Biol, 2008. **28**(17): p. 5369-80.